Bridging magnetothermal winds and photoevaporation to model discs dispersal

Giovanni Picogna[1]★ and Barbara Ercolano[1,2,3]
[1]*Universitäts-Sternwarte, Ludwig-Maximilians-Universität München, Scheinerstr. 1, D-81679 München, Germany*
[2]*Excellence Cluster Origins, Boltzmannstrasse 2, D-85748 Garching bei München, Germany*
[3]*Max-Planck-Institut für Extraterrestrische Physik, Giessenbachstr. 1, 85748 Garching, Germany*

arXiv:2609.18334v1 [astro-ph.EP] 16 Sep 2026

Draft – compiled 17 September 2026

ABSTRACT

Protoplanetary disc dispersal is driven by two processes usually modelled separately: photoevaporative and magnetohydrodynamic (MHD) disc winds. Global simulations indicate that in the inner disc these are not distinct outflows but a single magnetothermal wind. We assemble a closed-form, two-phase model that respects it. A single-field-line wind, whose base is fixed by the irradiated temperature and penetration column, supplies the launch and feeds a secular evolution, with photoevaporation convolved on as a sink. The flux closure $B_z \propto \Sigma^q$ is self-limiting: for $q \leq 1/2$ depletion alone cannot demagnetise the disc, so dispersal requires independent flux loss, parameterised by the magnetic Reynolds number $\mathcal{R}_m$. Integrating the coupled system yields two regimes. Efficient flux loss ($\mathcal{R}_m \lesssim 1$) lets the magnetisation front recede by over an order of magnitude and opens a photoevaporative gap. Flux retention ($\mathcal{R}_m \gg 1$) drives the front outward, sustains accretion, and defers dispersal by ≈ 2.7 Myr. Deriving the base from stellar irradiation instead of prescribing it, we find that the cold-launch approximation is valid during the early stages of disc evolution: anchoring the base at plasma equipartition ($\beta_{\rm base} \sim 1$) confines irradiation's influence on the magnetic lever arm to the magnetothermal annulus, decoupling the peak accretion rate from the incident flux. Both regimes clear the disc inside-out, through either a photoevaporatively amplified cavity wall or an expanding magnetothermal front.

Key words: accretion, accretion discs – magnetohydrodynamics (MHD) – protoplanetary discs – stars: winds, outflows

1 INTRODUCTION

The evolution, and eventual dispersal, of a protoplanetary disc is set by how efficiently it transports angular momentum and loses mass. Two pictures lead the recent literature. In the first, a turbulent ("viscous") stress drives accretion. A thermally launched photoevaporative wind, powered by stellar extreme-ultraviolet (EUV), far-ultraviolet (FUV) and X-ray irradiation, removes mass from the upper layers (Clarke et al. 2001; Alexander et al. 2006; Gorti & Hollenbach 2009; Owen et al. 2010, 2012; Picogna et al. 2019; Komaki et al. 2021). In the second, a large-scale magnetic field threading the disc exerts a torque that drives a magnetised wind, removing both mass and angular momentum (Blandford & Payne 1982; Ferreira 1997; Casse & Ferreira 2000a,b; Suzuki et al. 2016; Tabone et al. 2022). Both reproduce the two-timescale character of dispersal, set by stellar irradiation in the first case and by the initial disc magnetisation in the second (Armitage et al. 2013). Both are invoked to explain dispersal timescales and demographics (Pascucci et al. 2023). Observationally the two wind types are difficult to separate (especially once external photoevaporation is included, Facchini et al. 2016; Winter & Haworth 2022; Anania et al. 2025).

At the launch point, however, they are not separable mechanisms at all. Local and global non-ideal MHD simulations of the inner disc show the wind leaving several scale heights above the mid-plane, from layers that are simultaneously magnetically torqued, heated and ionised by FUV and X-ray photons (Bai et al. 2016; Bai 2017; Béthune et al. 2017; Wang et al. 2019; Gressel et al. 2020). This is the same non-ideal environment in which MRI turbulence is suppressed over much of the disc's lifetime, leaving the magnetised wind the only viable driver of the observed accretion rates (Bai 2017; Lesur 2021). Bai et al. (2016) termed the resulting outflow "magnetothermal": a single wind whose acceleration is shared between magnetic pressure and tension, and the thermal pressure of the irradiated surface gas. The cold magnetocentrifugal wind and the thermally dominated wind are the two end members of a continuum, not independent additive winds.

Models combining an MHD-wind torque with a separate photoevaporative mass sink already exist. The two terms can act at the same radii simultaneously, but each is computed from decoupled driving physics (Kunitomo et al. 2020; Weder et al. 2023; Coleman et al. 2024; Tabone et al. 2025). We propose a closed-form treatment that instead (i) sets the wind-launch thermodynamics from the same irradiation that drives photoevaporation, so the launch is genuinely magnetothermal as opposed to a superposed cold wind plus a thermal sink, and (ii) folds photoevaporation into the wind-driven secular evolution analytically. Its components are established: the single-field-line magnetothermal wind solver of Bai et al. (2016), the secular wind-driven operator of Tabone et al. (2022), and the Green's-function treatment of photoevaporation of Ruden (2004). The novelty is in how they are coupled.

★ E-mail: picogna@usm.lmu.de

© 2026 The Authors

Our central result is that how a disc disperses depends on whether and when it leaves the magnetothermal phase. If the vertical magnetic field is tied to the gas surface density through the standard closure $B_z \propto \Sigma^q$, the midplane plasma β (the ratio of the midplane thermal pressure to the poloidal magnetic pressure, $\beta = 8\pi P_{\rm mid}/B_z^2$ with $P_{\rm mid} = \Sigma c_{\rm s}\Omega/\sqrt{2\pi}$) evolves as:

$$\beta \propto \frac{\Sigma c_{\rm s}^2}{B_z^2} \propto \Sigma^{1-2q}, \tag{1}$$

at fixed midplane temperature. For $q \leq 1/2$, depletion alone cannot raise β enough to demagnetise the disc. The hand-over to photoevaporation-dominated dispersal is therefore not an automatic consequence of disc evolution. It requires genuine loss of magnetic flux.

That inequality is this paper's load-bearing assumption, and we do not derive it. q parametrises a flux transport the secular model does not solve. We adopt it because global non-ideal MHD calculations find the poloidal flux advected inward and concentrated instead of carried outward with the draining gas (Bai & Stone 2017; Suriano et al. 2018, 2019; Cui & Bai 2021; Lesur 2021). Were $q > 1/2$ instead, draining alone would demagnetise the disc. There would be no distinct flux-loss event, and the two branches below would collapse into one gas-depletion-driven transition. Section 4 sets out the evidence and its qualifications, Section 5.1 the fiducial value.

We parametrise that loss by a single global timescale τ_B,

$$\beta \propto \Sigma^{1-2q} \exp(t/\tau_B)\,, \tag{2}$$

so that $\tau_B \to \infty$ retains the flux and finite τ_B loses it. Here $\tau_B \sim R_{\rm disc}^2/\eta_{\rm eff}$ is the diffusion time set by the effective diffusivity of the poloidal induction equation, and is interchangeable with the magnetic Reynolds number $\mathcal{R}_m$ used throughout. $\mathcal{R}_m \gg 1$ means $\tau_B \to \infty$, and $\mathcal{R}_m \lesssim 1$ means τ_B short compared with the disc lifetime. It is a proxy for outward flux diffusion, not a solution of the induction equation.

As Armitage et al. (2013) first suggested, this splits the late evolution into two branches:

- if flux is efficiently lost ($\mathcal{R}_m \lesssim 1$), the magnetothermal driving weakens and internal photoevaporation can open a gap;
- if flux is retained ($\mathcal{R}_m \gg 1$), the field concentrates as the disc drains, accretion is sustained and dispersal deferred — the regime in which Martel & Lesur (2022) obtain an accreting cavity.

Photoevaporative dispersal is thus the outcome of the flux-losing branch specifically, not the default fate of every disc, and we make that choice the model's explicit control parameter.

Section 2 sets out the wind launch physics and fixes the magnetothermal wind base from photoevaporation physics; Section 3 constructs the Green's function of the wind operator and the photoevaporation convolution; Section 4 ties the magnetothermal front to the magnetic flux transport; Section 5 integrates the two flux-transport branches and analyses their evolution and dispersal. Throughout, the photoevaporation is the star's own: external (FUV-driven) photoevaporation is deliberately left out, and Section 6.3 sets out why, at what cost, and what would be needed to include it consistently. Section 6 compares our model with prior work and lists the caveats, and Section 7 gives our main conclusions.

2 THE PRIMORDIAL PHASE: THE MAGNETOTHERMAL WIND WITH AN IRRADIATION-SET BASE

We consider a disc around a star of mass M_*, with cylindrical radius R, Keplerian frequency $\Omega = \sqrt{GM_*/R^3}$, sound speed $c_{\rm s}$, and pressure scale height $H = c_{\rm s}/\Omega$. Table 1 shows all the adopted variables grouped by role.

Table 1. Quantities in the model, grouped by role, with the values adopted in Section 5.

Symbol	Meaning	Value or definition
Evolved field		
$\Sigma(R,t)$	disc surface density (dependent variable)	
Prescribed inputs		
M_*	stellar mass	$1\,M_\odot$
$M_{\rm disc}$	initial disc mass	$0.02\,M_\odot$
$\Sigma_0(R)$	initial surface density, $\propto (R/R_c)^{-1}e^{-R/R_c}$	$R_c = 30$ AU
$T_{\rm mid,0}$	passive mid-plane temperature at 1 AU	280 K
p	power law mid-plane temperature index	1/2
μ	mean molecular weight at the wind base	2.34 (molecular)
q	flux-closure index, $B_z \propto \Sigma^q$	0.3
p_B	wind-stress index, $\alpha_{\rm DW} \propto \beta^{-p_B}$	≈ 1
$q_{\rm div}$	field-divergence index (Sec. 2.1)	$\to \infty$ in eq. (13)
$\beta_0(R)$	initial mid-plane plasma-β	$30\,(R/{\rm AU})^{3/2}$
$\beta_{\rm crit}$	launch-cutoff plasma-β (midplane)	10^4
$\beta_{\rm couple}$	coupling-height plasma-β (local)	1
$\alpha_{\rm DW}^0$	wind transport coefficient, initial value	10^{-3}
$\alpha_{\rm DW}^{\rm max}$	ceiling on $\alpha_{\rm DW}$ (eq. 16)	1
$\alpha_{\rm SS}$	turbulent (viscous) α	10^{-5}
τ_B	flux-loss timescale (the branch control)	∞ / 0.5 Myr
$\mathcal{R}_m$	large-scale magnetic Reynolds number	set by τ_B
L_X	stellar X-ray luminosity	2×10^{30} erg s^{-1}
$N_{\rm b}$	radiation penetration column (eq. 10)	10^{21} cm^{-2}
$f_{{\rm gap},\sigma}$	depletion threshold defining $R_{\rm cav}$	0.05
Calculated (primordial-phase launch / identities)		
λ	magnetic lever arm, $(R_{\rm A}/R_0)^2$	derived (Sec. 2.1)
ξ	ejection index, $= 1/[2(\lambda-1)]$	derived
$z_0(R,t)$	wind-base height	$\min(z_{0,\rm th}, z_{0,\rm mag})$
ω_B	flux-decay index, $p_B(1-2q)$	0.4
Ξ	X-ray ionisation parameter	$L_X/(nr^2)$
$T_{\rm b}(R)$	irradiated wind-base temperature	Sec. 2.2
$\beta_{\rm base}$	plasma-β at z_0; sets λ	
$S(\beta)$	launch switch	eq. (17)
ψ	$\alpha_{\rm DW}/\alpha_{\rm SS}$; analytic limit assumes $\psi \gg 1$	
Diagnostics (from the evolving $\Sigma(R,t)$)		
$\beta(R,t)$	evolving mid-plane plasma-β	eq. (26)
$R_\beta(t)$	magnetisation front	
$R_{\rm c}(t)$	photoevaporation cut-off radius	
$R_{\rm gap}(t)$	photoevaporation gap front (rate-based)	
$R_{\rm cav}(t)$	inner-cavity edge (density-based)	
$\dot M_*(t)$	stellar accretion rate, $\equiv \dot M_{\rm acc}$	

The central quantity is the magnetic lever arm $\lambda \equiv (R_{\rm A}/R_0)^2$, the squared ratio of the Alfvén radius to the launch radius on a wind field line (Blandford & Payne 1982). In a radially self-similar accretion–ejection flow the wind-driven mass loss and accretion are related through the ejection index

$$\xi \equiv \left.\frac{{\rm d}\dot M_{\rm w}/{\rm d}\ln R}{\dot M_{\rm acc}}\right|_{R_0} = \frac{1}{2(\lambda-1)}, \tag{3}$$

(Ferreira 1997; Bai et al. 2016). The launch calculation of Section 2 returns ξ (hence λ), and the secular evolution of Section 3 adopts the same ξ as its wind mass-loss coefficient.

We construct the launch calculation in three steps. Section 2.1 sets out the single-field-line solution that returns λ from a prescribed base state. Section 2.2 fixes the base state itself from the irradiation and

magnetic-coupling conditions at the disc surface. Section 2.3 then collects the resulting wind properties and their limiting behaviour.

2.1 The single-field-line solution

We model the wind launching mechanism using the single-field-line formulation of Bai et al. (2016), which reduces the steady, axisymmetric, ideal-MHD equations to one-dimensional conservation laws along a prescribed poloidal field line (Weber & Davis 1967; Spruit 1996).

The field line is straight, of inclination θ measured from the disc mid-plane, so that arc length s from the base (R_0, z_0) traces $R(s) = R_0 + s\cos\theta$, $z(s) = z_0 + s\sin\theta$. The poloidal field strength along it is prescribed to steepen from parallel ($B_\mathrm{p} \propto R^{-1}$) to diverging ($\propto R^{-2}$) geometry, with the transition set by a parameter q_div. Under this kinematic prescription $\nabla\cdot\mathbf{B} = 0$ ties $B_\mathrm{p}(s)$ to the flux-tube cross-section. This means q_div governs how neighbouring field lines diverge, and the full trans-field force balance need not be solved. The transition sits at roughly $q_\mathrm{div}^{-1/2}R_0$. For their fiducial $q_\mathrm{div} = 0.25$ (transition at $\simeq 2R_0$) Bai et al. (2016) find that the Alfvén radius varies by a factor of a few across their parameter space.

In Gaussian cgs units, continuity, induction and azimuthal momentum give three constants along the line: the mass loading k, the field-line angular velocity ω, and the specific angular momentum l,

$$k = \frac{4\pi\rho v_\mathrm{p}}{B_\mathrm{p}}, \quad \omega = \frac{v_\phi}{R} - \frac{kB_\phi}{4\pi\rho R}, \quad l = Rv_\phi - \frac{RB_\phi}{k}, \tag{4}$$

with ρ the gas density, v_p and v_ϕ the poloidal and azimuthal fluid speeds, and B_ϕ the toroidal field. At the base $B_\phi = 0$ and the field co-rotates, so $\omega \simeq \Omega_\mathrm{K}(R_0)$, but v_ϕ/R departs from it downstream as the Maxwell stress spins the gas up. The energy equation supplies a fourth constant, the Bernoulli function

$$E = \tfrac{1}{2}\left(v_\mathrm{p}^2 + v_\phi^2\right) + \mathcal{H} - \frac{GM_*}{r} - \frac{\omega R B_\phi}{k}, \tag{5}$$

with r the spherical radius, in which thermodynamics enters only through the enthalpy $\mathcal{H} = \int \mathrm{d}P/\rho$ and the last term is the work done by the magnetic torque (Blandford & Payne 1982; Spruit 1996). For the isothermal closure $P = \rho c_\mathrm{s,w}^2$ adopted by Bai et al. (2016), $\mathcal{H} = c_\mathrm{s,w}^2 \ln\rho$, so the entire thermal content of the problem is carried by the single base sound speed $c_\mathrm{s,w}$.

The standard reduction (Weber & Davis 1967; Spruit 1996) eliminates B_ϕ between the invariants and casts the flow as one algebraic relation along the line in the variable $x \equiv v_\mathrm{Ap}^2/v_\mathrm{p}^2$, the squared ratio of the poloidal Alfvén speed to the flow speed. That relation is singular where $x = 1$, and finiteness of v_ϕ there forces $l = \omega R_\mathrm{A}^2$, with R_A the cylindrical radius of the Alfvén crossing. This is the sense in which the wind's angular momentum sets its lever arm $\lambda = (R_\mathrm{A}/R_0)^2$: the conserved l and ω, both fixed at the base, determine where the Alfvén surface must sit. Requiring the flow to pass smoothly through the slow and fast magnetosonic points in addition imposes three conditions on two unknowns at each critical point, so the problem is an eigenvalue problem. The mass loading k and the Alfvén radius R_A are not free: ω and E select them, and hence so do the base conditions.

This is the property the rest of the paper relies on. Given a footpoint (R_0, z_0) and the base state $(c_\mathrm{s,w}, \rho_0, B_\mathrm{p0}, \theta)$, the solver returns the lever arm $\lambda = (R_\mathrm{A}/R_0)^2$, and with it the ejection index ξ through equation (3), the wind mass flux, and the surface torque. Rather than solve the full eigenvalue problem at every footpoint, we read the lever arm per cell off the Bai et al. (2016) solution family (his Fig. 5). This collapses onto a single monotone function $\lambda(\beta_\mathrm{base})$ of the wind-base plasma-β, $\beta_\mathrm{base} = \beta_\mathrm{mid}(c_\mathrm{s,w}^2/c_\mathrm{s}^2)\exp[-(z_0/H)^2/2]$ (the mid-plane β scaled to the anchor height z_0). Because $c_\mathrm{s,w}$ and z_0 are set per cell by the irradiation and magnetic-coupling conditions at the disc surface, λ (and hence ξ) responds self-consistently to the wind-base state as the disc evolves. A hotter or more depleted base raises β_base and lowers λ; a cooler or less depleted base raises it. For the fiducial disc at $t = 0$ the derived λ runs from 6.8 ($\xi = 0.086$) across the inner launching region to 5.2 ($\xi = 0.12$) at the magnetisation front, and the two branches then drive it apart. Section 5.5 follows that evolution.

Because the map is a digitisation of a published figure, its calibration range bounds where λ is interpolated instead of extrapolated. Bai's Fig. 5 spans $\beta_\mathrm{base} = 2.5\times10^{-4}$ to 160. The low-β end is never approached: wherever the base is set magnetically, $\beta_\mathrm{base} = 1$ by the definition of $z_\mathrm{0,mag}$, four decades above the tabulated minimum. At the high-β end, measured over the launching region where λ has any effect, every cell and all of the mass lie inside the tabulated range on the flux-loss branch at every epoch: β_base there never exceeds 7.7, five per cent of the upper bound. On the flux-retained branch the same holds through $t = 5$ Myr, where the maximum reaches 91. Only in that branch's final Myr does it cross: at 5.5 Myr, five of 192 launching cells, carrying 8 per cent of the launching region's mass, reach $\beta_\mathrm{base} \approx 230$. Beyond the tabulated range the map continues smoothly onto the weak-field Blandford–Payne limit $\lambda \to 3/2$ instead of clamping, so those cells are extrapolated, not pinned. The window in which they appear is the one Appendix F1 already excludes on resolution grounds.

2.2 Fixing the base from photoevaporation physics

The single-field-line solution of Section 2.1 takes the base sound speed $c_\mathrm{s,w}$ and the base height z_0 as free parameters. Fixing both per streamline, from the local irradiation and magnetic-coupling conditions, is what makes the launch magnetothermal, and is where photoevaporation physics enters the wind solution. Because each field line is solved independently, no global temperature profile is imposed. The strict self-similarity of the classical accretion–ejection structures (Ferreira 1997; Casse & Ferreira 2000b) is relaxed, and each footpoint carries its own base temperature.

2.2.1 The base temperature

The wind-base sound speed follows from the irradiated base temperature,

$$c_\mathrm{s,w}(R_0) = \sqrt{\frac{k_\mathrm{B}\,T_\mathrm{b}(R_0)}{\mu m_\mathrm{H}}}, \tag{6}$$

where k_B is the Boltzmann constant, m_H the hydrogen mass, T_b the irradiated base temperature, and μ the mean molecular weight. The base sits at the sharp vertical gradient where FUV/X-ray heating overcomes line cooling (Wang et al. 2019; Sarafidou et al. 2024).

We take the molecular $\mu = 2.34$ throughout the internally irradiated base. The Sellek et al. (2024) Ξ–T relation adopted below returns $T_\mathrm{b} = 95$–450 K over 0.5–200 AU at the penetration column $N_\mathrm{b} = 10^{21}\,\mathrm{cm}^{-2}$ that defines the base (Appendix A, panel c). Over that range hydrogen is neither dissociated nor ionised, and the same models report H_2 surviving into the wind as its dominant coolant at tens of AU. The non-ideal MHD wind-launching literature the Section 2.1 closure is drawn from likewise takes the launching region to be molecular (e.g. Bai et al. 2016; Gressel et al. 2020). A fully ionised $\mu = 0.65$ would overstate $c_\mathrm{s,w}^2$ by a factor 3.6. The one exception is the escape temperature of equation (7), which retains the

ionised value where its 10^4 K ceiling binds and the gas genuinely is ionised.

We set T_b from the local X-ray ionisation state instead of prescribing it. Writing the ionisation parameter as $\Xi \equiv L_X/(nr^2)$ (Tarter et al. 1969), with n the number density at the base and r the distance from the star, we adopt the empirical Ξ–T relation of Sellek et al. (2024). We take $L_X = 2 \times 10^{30}$ erg s^{-1}, consistent with the $\log L_X$–$\log M_*$ relation of Güdel et al. (2007) at $M_* = 1\,M_\odot$. The same radiation field and the same local density then drive both the wind-base thermodynamics and the photoevaporative mass loss, instead of entering as independent inputs. Since $\Xi \propto 1/\Sigma$, an instantaneous $\Sigma \to T_b$ closure would let the base temperature respond to depletion without limit. We therefore relax T_b toward its equilibrium value over the local recombination time $\tau_{rec} = 1/(\alpha_r(T)n)$, with α_r the hydrogenic radiative recombination coefficient (Verner & Ferland 1996), so the gas cannot reconfigure faster than it can recombine. For the same reason we do not extrapolate the Ξ–T relation outside the density range it was fitted over: below $\Sigma/\Sigma_0 = 10^{-2}$ the base is blended smoothly back to T_{mid}. That blend bites only late and only where the disc is nearly empty. By $t \approx 3.5$ Myr the flux-loss branch has $\Sigma/\Sigma_0 \sim 10^{-4}$ inside a few AU, so its base sits on the mid-plane temperature even though the irradiation front has reached it. It errs in one direction only: $\Xi \propto 1/\Sigma$ implies that gas should in reality be hotter than the mid-plane, so the late inner disc is under-heated, not over-heated. Appendix A gives the numerical treatment and the sensitivity of the results to it.

Whether that base can drive a wind on its own is set by the escape condition

$$T_{esc}(R) = \frac{\mu m_H G M_*}{k_B R} \propto R^{-1}. \tag{7}$$

Gas at $T_b = T_{esc}$ has $c_{s,w} = v_K$, i.e. $\varepsilon_b \equiv c_{s,w}/v_K = 1$: the condition under which a purely thermal wind is self-launching. Thermal winds in practice launch from well inside the radius at which it is met (Owen et al. 2012), and we evaluate the base temperature from the Ξ–T relation above, at the launch column, so

$$\varepsilon_b(R,t) = \left[\frac{T_b(R,t)}{T_{esc}(R)}\right]^{1/2} \tag{8}$$

is a local, evolving diagnostic rather than a fixed radius.

Photoionised gas equilibrates near 10^4 K. The photoelectrons carry only the excess energy above the 13.6 eV hydrogen ionisation threshold, and balancing that heating against recombination and collisionally excited line cooling fixes the equilibrium temperature at $\sim 10^4$ K, largely independently of the ionising spectrum and luminosity (Osterbrock & Ferland 2006). The Ξ–T relation recovers this asymptote, so the fiducial base temperature is bounded without an artificial cap.

2.2.2 *The base height*

The launch surface is not a static geometric boundary. In X-ray-heated non-ideal MHD simulations the outflow originates from an extended vertical transition zone, and two thresholds are crossed at different heights. Above $z_{0,th}$ the gas is hot enough to be irradiation-heated, and above $z_{0,mag}$ it is well enough coupled to the field for the ideal-MHD invariants of Section 2.1 to apply. Neither is individually necessary for an outflow. Material launched from a coupled but as-yet-unheated layer leaves as a cold magnetocentrifugal wind and is heated as it rises. The converse state (heated but as-yet-uncoupled) is harder to sustain, because the photons that heat the surface layer also ionise it. FUV photoionisation of trace species maintains $x_e \sim 10^{-5}$ in the heated layer (Perez-Becker & Chiang 2011). Non-ideal MHD calculations that solve the thermochemistry alongside the diffusivities find the irradiated surface to be well enough coupled to launch, instead of a decoupled layer that leaves thermally (Gressel et al. 2015, 2020). We therefore do not read the two thresholds as selecting between magnetic and thermal driving. The base is simply the lower of the two,

$$z_0(R_0) = \min\left(z_{0,th},\, z_{0,mag}\right), \tag{9}$$

and which of the two is binding fixes the thermodynamic character of the base, not the identity of the driving mechanism. Where $z_{0,mag} < z_{0,th}$ the base lies below the irradiation front. The gas is launched cold and magnetocentrifugally and is heated only once it has risen past $z_{0,th}$, so the irradiation adds neither mass loading nor angular-momentum extraction at the base. Where $z_{0,th} < z_{0,mag}$ the base sits at the front itself. The launch is genuinely magnetothermal, and the elevated base temperature raises $c_{s,w}$ and with it the mass loading, lowering the lever arm λ.

On the flux-retained branch $z_{0,mag} < z_{0,th}$ over 72 per cent of the launching region at $t = 0$, falling to 64 per cent by 5 Myr. Taking the minimum therefore places the base below the irradiation front over most of the disc, whereas Bai & Stone (2013) and Bai et al. (2016) identify the base with the FUV front itself. Recent global simulations support the former. Carrying all three non-ideal terms with radiation transport, Mori et al. (2025) find that "wind launching can take place in regions where gas is not fully coupled to magnetic field with Am $\gtrsim 1$", below an FUV front that in their calculation "is located high in the atmosphere". Launching from marginally coupled gas beneath the front is what equation (9) does by construction. The two prescriptions coincide precisely where the remaining third of the disc sits, in the magnetothermal annulus.

This is not the magnetothermal-to-thermal boundary. That boundary is set by the field, as opposed to the base. The outflow is magnetically driven only while $\beta < \beta_{crit}$, that is inside the magnetisation front R_β; beyond it the wind is purely thermal. Because the radial column falls and β rises outward, $z_{0,th}$ decreases and $z_{0,mag}$ increases with R. The disc therefore divides into three regions: an inner cold magnetocentrifugal launch, an intermediate magnetothermal band between the base crossover $z_{0,th} = z_{0,mag}$ and R_β, and thermal photoevaporation beyond R_β (Figure 1). The two radii are related but distinct, and their ordering (and hence the width of the magnetothermal band) is a result of the evolution, not an input.

The *thermal base* $z_{0,th}$ sits where stellar X-ray/EUV irradiation penetrates to the heating column $N_X \approx 10^{21}$–10^{22} cm^{-2} (Ercolano et al. 2009). Because this radiation grazes the disc from the central star, the attenuating column is the radial, not the vertical, one. For a hydrostatic Gaussian interior of scale height $H = c_s/\Omega$ and nominal mid-plane H-nucleus density $n_{mid} = \Sigma/(\sqrt{2\pi} H m_H)$, the column to the point (R, z) along a ray of constant opening $u \equiv z/R$ is

$$N_{rad}(R,u) = \int_0^R n_{mid}(r)\, \exp\left[-\frac{(u\,r)^2}{2H(r)^2}\right] \sqrt{1+u^2}\, dr, \tag{10}$$

which decreases monotonically with u; $z_{0,th}(R) = u_\star R$ where $N_{rad}(R, u_\star) = N_X$. We adopt the lower bound of that range, $N_X = 10^{21}$ cm^{-2}, and evaluate equation (10) with the column scaled by the proton mass, Σ/m_H.[1] Since N_{rad} is linear in n_{mid}, this is exactly equivalent to using the true H-nucleus density with a threshold $N_X = 10^{21}/\mu_H \simeq 7 \times 10^{20}$ cm^{-2}. Because the uncertainty on N_X

[1] The mean mass per hydrogen nucleus is $\mu_H m_H$ with $\mu_H \simeq 1.4$, distinct from the mean mass per free particle μm_H ($\mu = 2.34$) that sets the sound speed.

itself spans an order of magnitude, the factor 1.4 is absorbed into that choice rather than left as an uncorrected offset. The lower integration limit in equation (10) accounts for attenuation by disc material interior to the computational domain. We extrapolate the initial surface density profile Σ_0 inwards to a magnetospheric truncation radius of ~ 0.05 AU, scaled to the time-dependent surface density at the inner boundary so that the inner shadow recedes as the disc drains. Neglecting it would expose the innermost grid cells to midplane ionising radiation and collapse $z_{0,\rm th}$ unphysically. Beyond $R_{\rm c}(t)$ the unshadowed line of sight assumed by Ξ breaks down, and there $T_{\rm b}$ reverts to the midplane temperature, a strict lower bound on the wind-base kinematics, justified in Appendix A.

The *magnetic base* $z_{0,\rm mag}$ marks the base of the magnetically dominated region. Above it the magnetic energy density exceeds the thermal, gravitational and kinetic energy densities of the gas, so the poloidal velocity aligns with the poloidal field. This is the approximation on which the single-field-line solution of Section 2.1 rests. Assuming a vertically isothermal Gaussian density profile and a constant B_z, the plasma-β scales as $\beta(z) = \beta(R,t)\, e^{-z^2/2H^2}$. Imposing equipartition, $\beta(z_{0,\rm mag}) = \beta_{\rm couple} \sim 1$, yields

$$z_{0,\rm mag} = H\sqrt{2\ln\!\left[\beta(R,t)/\beta_{\rm couple}\right]}, \tag{11}$$

which is set to zero if the midplane is already magnetically dominated ($\beta(R,t) \le \beta_{\rm couple}$). Equation (11) is our own construction, and is not the definition of the wind base adopted by the works whose launch physics we use. Both Bai & Stone (2013) and Bai et al. (2016) place the base at the height where the azimuthal velocity turns from sub- to super-Keplerian, marking the onset of centrifugal acceleration. Bai et al. (2016) takes that height as an input boundary condition instead of deriving it. The two criteria are nevertheless the same transition seen from opposite sides. Gas below the base is sub-Keplerian because it is pressure supported, and turns super-Keplerian when the magnetic torque overcomes that support, which occurs where the magnetic and thermal energy densities cross, $\beta \sim 1$. Equation (11) is thus an analytic proxy for a height we do not otherwise compute, since this vertically integrated treatment carries no $v_\phi(z)$. The proxy can be tested two ways. Quantitatively, the fiducial run of Bai & Stone (2013) has a midplane $\beta_0 = 10^5$ and measures its wind base at $z_{\rm b} \simeq 4.69\,H$. Equation (11) with $\beta_{\rm couple} = 1$ gives $H\sqrt{2\ln 10^5} = 4.80\,H$, agreeing to 2.3 per cent with no free parameter. Independently, the two-dimensional global simulations of Mori et al. (2025), which carry all three non-ideal terms (Ohmic, Hall and ambipolar) together with radiation transport, report that in their Hall-free run "wind launching empirically occurs around the region where the magnetic pressure dominates over the thermal pressure (i.e., plasma $\beta \sim 1$)". Our $\beta_{\rm couple} = 1$ is therefore not a convenient choice but the launching surface those calculations find, and we adopt it on that basis.

Whether the gas is coupled to the field well enough to drive a wind at all is a separate requirement. This model does not evaluate it. Semi-analytic wind-driving disc solutions exist only above an ambipolar Elsasser number $\Lambda_{\rm A} \gtrsim 1$ (Wardle & Koenigl 1993; Königl & Salmeron 2011). Published simulations of discs of this type satisfy that bound over the launching region, and Section 6.3 gives the evidence together with what it does not cover. A consistent anchor would be set by $\Lambda_{\rm A}$ in place of β, which a vertically integrated model carrying no ionisation network cannot compute. Varying how the two thresholds of equation (9) are combined moves the integrated results by only a few per cent. That bounds the sensitivity to where the anchor sits, but not to the criterion that defines it.

The isothermal-Gaussian assumption sets a strict lower limit on the base height. In irradiated discs the heated surface layers decay far more gradually than a Gaussian, so the true $\beta(z)$ falls more slowly and the physical coupling transition lies higher in the atmosphere. The model's topology limits how far that error propagates. The Gaussian fails in the heated layer above the thermal base, $z > z_{0,\rm th}$. Where the base is magnetically anchored ($z_{0,\rm mag} < z_{0,\rm th}$) the wind anchors in the shielded interior, where the isothermal assumption holds. Because $\beta_{\rm base} = \beta_{\rm couple}$ by definition in those cells, the lever arm λ and the mass loading ξ follow from the coupling criterion alone, independently of the assumed vertical density profile. Where the isothermal estimate instead places the magnetic base inside the heated layer ($z_{0,\rm mag} > z_{0,\rm th}$), the minimum in equation (9) defaults to the thermal threshold and bounds the launch height. The validity of this assumption breaks down within the thermally anchored cells. There $\beta_{\rm base}$ is evaluated on the Gaussian at $z_{0,\rm th}/H \simeq 3.5$–$5.5$, and the density underestimate propagates directly into λ and ξ. A flared atmosphere would raise $\beta_{\rm base}$, lower λ, and lift $z_{0,\rm mag}$, moving further cells into the thermally anchored regime and compounding the error. Correcting it requires the vertical temperature structure, which a vertically integrated model does not carry. This is the principal structural limitation of the base prescription.

Equations (9)–(11) make the base height a function of the local surface density and field strength, and so couple the launch directly to the disc secular evolution. Figure 1 shows schematically the resulting geometry.

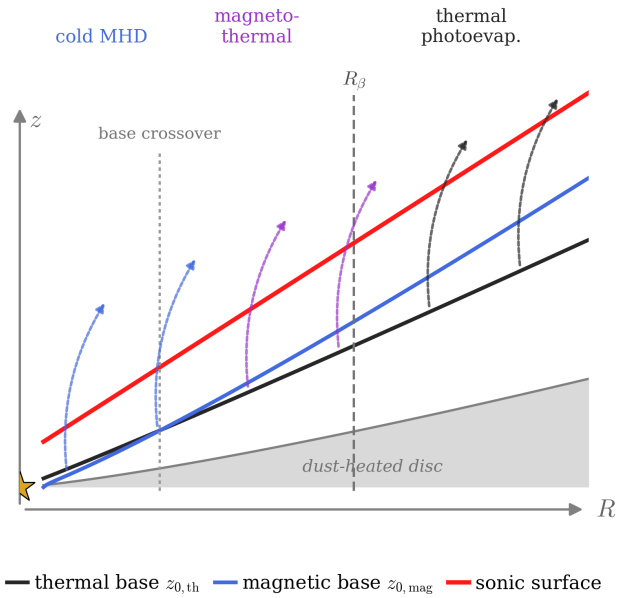

Figure 1. Schematic vertical structure of the magnetothermal wind base, divided by radius into three regimes: an inner cold magnetocentrifugal launch, an intermediate magnetothermal band bounded by the base crossover $z_{0,\rm th} = z_{0,\rm mag}$ and the magnetisation front R_β, and thermal photoevaporation beyond R_β (Section 2.2).

2.2.3 *Secular behaviour and scope*

Because the base thresholds depend on local surface density and field strength, the launch kinematics couple directly to the disc's secular evolution. As the disc drains, the radial column drops below the penetration depth $N_{\rm X}$ and drives $z_{0,\rm th}$ toward the mid-plane. However,

irradiation alone only moves the launch height. Changing the launch mechanism requires magnetic flux loss. If flux dissipates (finite τ_B), the mid-plane β rises, driving $z_{0,\rm mag}$ higher and forcing the magnetisation front R_β (where $\beta = \beta_{\rm crit}$) to recede. As Figure 1 shows, this sweeps the disc from a magnetically driven outflow, through a mixed state, to a purely thermal wind. If instead flux is retained ($\tau_B \to \infty$), R_β expands and the outflow stays magnetically driven for the disc's entire lifetime.

2.3 Wind properties and the cold (Blandford–Payne) limit

For each footpoint the converged solution returns the dimensionless mass loading $\mu_{\rm w} = \omega R_0 k/B_{\rm p0}$, the lever arm λ, and the surface-torque accretion and wind mass-loss rates formulated by Bai et al. (2016):

$$\dot{M}_{\rm acc} = \frac{2R_0}{\Omega_{\rm K}(R_0)} B_{\rm p0}^2 \left|\frac{B_\phi}{B_{\rm p}}\right|_{z_0} \sin\theta, \qquad \frac{{\rm d}\dot{M}_{\rm w}}{{\rm d}\ln R} = 2\pi R_0^2 \rho_0 v_{\rm p0}, \tag{12}$$

with $B_z = B_{\rm p}\sin\theta$ for the equatorial convention on θ. The ratio of these rates reproduces the ejection index ξ only to within $\sim 10\%$, because the torque formulation assumes a strictly co-rotating base (Wardle & Koenigl 1993) that the solved v_ϕ violates slightly (Bai et al. 2016, footnote 9). We therefore extract ξ directly from the exact angular-momentum balance in equation (3), which needs neither the launch-surface area element nor the field inclination.

The mass loading $\mu_{\rm w}$ is dimensionless under a unit base density normalisation, and single-field-line models fix kinematic ratios (λ, ξ, and velocity profiles) but not the absolute mass flux. $\dot{\Sigma} = 2\rho_0 v_{\rm p0}$ scales with the base density, which here is set to enforce the $\beta_{\rm couple}$ height condition (equation 11), not to calibrate a physical mass-loss rate. We therefore take only the robustly determined λ from the local solution, prescribe $\alpha_{\rm DW}$, and compute the wind mass loss through the transport sink (equation 14).

In the cold limit ($c_{\rm s,w} \to 0$, $q_{\rm div} \to \infty$, $\theta = 0$, $z_0 \to 0$), the solution collapses to the Spruit (1996) relations:

$$\lambda = \tfrac{3}{2}\left(1 + \mu_{\rm w}^{-2/3}\right), \qquad \frac{v_{\rm p}^\infty}{\omega R_0} = \mu_{\rm w}^{-1/3}. \tag{13}$$

This limit is algebraically identical to the self-similar cold family of Blandford & Payne (1982), yielding their invariant $\beta_{\rm BP} = \mu_{\rm w}(2\lambda - 3)^{3/2} = 3^{3/2} \simeq 5.20$. Our $\mu_{\rm w}$ matches Spruit's dimensionless mass flux exactly, and aligns with the κ of Martel & Lesur (2022) by excluding the base-inclination factor $1/\sin\theta_0$ present in Blandford & Payne's original definition.

This cold relation is also what carries the lever arm outside the magnetised disc. Beyond the magnetisation front the launch switch turns off, and λ follows the $\lambda(\mu_{\rm w})$ of equation (13) continuously, as opposed to the $\beta_{\rm base}$ map of Section 2.1. We apply it there because it is continuous and has the right weak-field limit, not because it is calibrated there: outside the magnetically dominated regime it is a functional form, not a calibrated relation.

Two constraints bound its use. First, it assumes $q_{\rm div} \to \infty$; finite values (e.g. $q_{\rm div} = 0.25$) preserve the functional form but introduce a zero-point offset (Bai et al. 2016). Second, it enforces $\lambda > 3/2$, so $\xi < 1$ always. A weakening magnetic field therefore drives the system toward higher mass loss per unit accretion, the inverse of what an outer-disc conveyor feeding an inner cavity requires. It remains a purely cold relation, omitting the thermal driving that raises $c_{\rm s,w}$ at the base (Discussion Caveat 1).

3 THE PRIMORDIAL PHASE: SECULAR EVOLUTION AND THE PHOTOEVAPORATION SINK

3.1 The wind-driven operator

The secular surface density evolves according to the Tabone et al. (2022) master equation:

$$\frac{\partial\Sigma}{\partial t} = \frac{3}{R}\frac{\partial}{\partial R}\left[\frac{1}{R\Omega}\frac{\partial}{\partial R}\left(R^2\alpha_{\rm SS}\Sigma c_{\rm s}^2\right)\right] + \frac{3}{2R}\frac{\partial}{\partial R}\left[\frac{\alpha_{\rm DW}\Sigma c_{\rm s}^2}{\Omega}\right] - \frac{3\alpha_{\rm DW}\Sigma c_{\rm s}^2}{4(\lambda-1)R^2\Omega} - [1 - S(\beta)]\,\dot{\Sigma}_{\rm PE}(R,t). \tag{14}$$

The first term is the Lynden-Bell & Pringle (1974) viscous (diffusive) operator with $\nu = \alpha_{\rm SS} c_{\rm s}^2/\Omega$. The second is the wind torque, a first-order (advective) term equivalent to an inward velocity

$$v_{\rm DW} = \frac{3}{2}\frac{\alpha_{\rm DW} c_{\rm s}^2}{R\Omega} = \frac{3}{2}\alpha_{\rm DW}\frac{c_{\rm s}^2}{v_{\rm K}}. \tag{15}$$

The third is the wind mass loss, which is linear in Σ and equal to $\dot{\Sigma}_{\rm DW} = \xi\, v_{\rm DW}\Sigma/R$ with the same ξ as equation (3). The fourth is the internal photoevaporation sink.

The transport coefficient $\alpha_{\rm DW}$ is not a static normalisation but evolves with the disc:

$$\alpha_{\rm DW}(R,t) = \min\left[\alpha_{\rm DW}^0\left(\frac{\Sigma}{\Sigma_0}\right)^{-(1-2q)},\ \alpha_{\rm DW}^{\rm max}\right] S(\beta)\, S_{\rm th}, \tag{16}$$

in which the depletion factor $(\Sigma/\Sigma_0)^{-(1-2q)}$ follows from the field–surface-density closure of eq. 1 and strengthens the torque as the disc drains. $\alpha_{\rm DW}^{\rm max} = 1$ imposes a physical Maxwell-stress ceiling. $S_{\rm th}$ cuts off the wind if the base collapses to the mid-plane. The magnetic switch,

$$S(\beta) = [1 + \beta/\beta_{\rm crit}]^{-1}, \tag{17}$$

terminates the outflow for weak fields ($\beta \gg \beta_{\rm crit}$).

Because $\beta \propto \Sigma^{1-2q}$ (equation 1), the depletion factor scales exactly as β^{-1}. In the active launching region ($\beta < \beta_{\rm crit}$ where $S \to 1$), this recovers the $\alpha_{\rm DW} \propto \beta^{-1}$ wind-stress scaling measured in non-ideal MHD simulations (Bai & Stone 2013; Bai et al. 2016; Lesur 2021). In the weak-field limit, $S(\beta)$ imposes a second power, steepening the fall-off to $\alpha_{\rm DW} \propto \beta^{-2}$. We choose the linear switch because it gives the shallowest available rolloff. A steeper cutoff would artificially suppress the residual outer-disc torque.

Weighting the photoevaporative sink by $1 - S(\beta)$ enforces a unified outflow. Above the physical base z_0, mass loading is conserved along the field line. Irradiation heats gas the magnetic base has already lofted, setting $\beta_{\rm base}$ and with it the kinematic parameters (λ, ξ). Adding $\dot{\Sigma}_{\rm PE}$ directly to $\dot{\Sigma}_{\rm DW}$ would count that same gas twice. The magnetisation therefore paces the total mass loss: the outflow acts as a magnetothermal wind ($S \to 1$) at low β, and reverts smoothly to pure photoevaporation ($S \to 0$) at high β. This matches the radiation-magnetohydrodynamic results of Sarafidou et al. (2024), who find the total mass-loss rate transitions between the two regimes instead of summing them.

3.2 Closing the launch–evolution coupling

Equating the Tabone et al. (2022) advective flux, $\dot{M}_{\rm acc} = 2\pi R\Sigma v_{\rm DW} = 3\pi\alpha_{\rm DW}\Sigma c_{\rm s}^2 R/v_{\rm K}$, with the Bai et al. (2016) surface Maxwell torque, $\dot{M}_{\rm acc} = (2R/\Omega)|B_z B_\phi|_{z_0}$, yields the transport coefficient:

$$\alpha_{\rm DW} = \frac{2}{3\pi}\frac{R\, B_{\rm p0}^2 |B_\phi/B_{\rm p}|_{z_0}\sin\theta}{\Sigma c_{\rm s}^2}. \tag{18}$$

This identifies $\alpha_{\rm DW}$ as the surface Maxwell stress normalised by the column thermal energy density. Instead of recomputing $\alpha_{\rm DW}$ from the local stress at every radius and timestep, we anchor it to a global initial normalisation $\alpha^0_{\rm DW} = 10^{-3}$ (Table 1) and evolve it through equation (16). Because the closure forces $\alpha_{\rm DW} \propto \Sigma^{-(1-2q)}$, the torque strengthens as the disc drains. This is the explicit mechanism driving rapid terminal collapse on the flux-retained branch. The ejection index ξ, by contrast, is derived continuously from the local angular-momentum balance (equation 3) and fed straight into the secular mass-loss sink.

Parameterising one quantity globally while deriving the other locally is necessary because the two models account for mass inconsistently. The local launch solution's absolute mass flux, $\dot{\Sigma} = 2\rho_0 v_{\rm p0}$, differs from the secular transport sink, $\xi v_{\rm DW}\Sigma/R$, by over three orders of magnitude across the disc. This is because the 1D vertical model's base density is a construct adopted to enforce the $\beta_{\rm couple}$ height condition (equation 11) and carries no connection to the physical Σ the secular model tracks. We therefore keep only the kinematic ratios the launch solution determines reliably (λ, ξ), and discard its unnormalised absolute mass flux.

3.3 Characteristics and the Green's function

In the wind-dominated regime ($\psi \equiv \alpha_{\rm DW}/\alpha_{\rm SS} \gg 1$), the diffusive term becomes negligible and equation (14) reduces to a first-order hyperbolic equation with linear sinks. We adopt the irradiated passive-disc profile $c_{\rm s}^2 = c_{\rm s}^2(R_{\rm n})(R/R_{\rm n})^{-1/2}$, departing from the classical self-similar $c_{\rm s}^2 \propto R^{-1}$ of magnetised accretion-ejection structures. Under this profile the ratio $c_{\rm s}^2/v_{\rm K}$ is constant, so $v_{\rm DW} = \frac{3}{2}\alpha_{\rm DW}c_{\rm s}^2/v_{\rm K}$ becomes radius-independent if $\alpha_{\rm DW}$ is constant. (Because equation 18 gives $\alpha_{\rm DW} \propto RB_z^2/(\Sigma c_{\rm s}^2)$, a strictly uniform $\alpha_{\rm DW}$ with $\Sigma \propto R^{\xi-1}$ demands $B_z \propto R^{(2\xi-5)/4}$. We do not enforce this B_z dynamically, but treat $\alpha_{\rm DW}$ as a uniform parameter. The derivations below hold locally along characteristics even where $B_z(R)$ departs from this profile.)

The accretion characteristics are then straight lines:

$$\frac{{\rm d}R}{{\rm d}t} = -A, \quad R(t) = R_i - A\,t, \qquad A \equiv \frac{3}{2}\alpha_{\rm DW}\frac{c_{\rm s}^2(R_{\rm n})\sqrt{R_{\rm n}}}{\sqrt{GM_*}}. \tag{19}$$

This describes finite-time, non-spreading accretion: an annulus reaches the inner boundary in $t \sim R_i/A$. Along a characteristic, ${\rm d}\Sigma/{\rm d}R = (\xi-1)\Sigma/R$, yielding the homogeneous solution:

$$\Sigma(R) \propto R^{\xi-1}. \tag{20}$$

For a general base scaling $c_{\rm s}^2 \propto R^{-p}$, the slope is $\xi + p - \frac{3}{2}$, recovering the classical self-similar $\xi - \frac{1}{2}$ at $p = 1$, and $\xi - 1$ for our irradiated $p = \frac{1}{2}$. The secular transport therefore recovers the steady-wind surface-density scaling implied by the local launch solution, which is an internal consistency check on the coupling.

Including the photoevaporation sink, the full transport along a characteristic is ${\rm d}\Sigma/{\rm d}t = \mathcal{D}(R)\Sigma - [1 - S(\beta)]\dot{\Sigma}_{\rm PE}$, with $\mathcal{D}(R) = A(1-\xi)R^{-1}$. Its integrating-factor solution provides the Green's function:

$$\Sigma(R(t)) = \frac{1}{\mathcal{I}(t)}\left[\Sigma_i - \int_0^t \mathcal{I}(t')\,[1 - S]\,\dot{\Sigma}_{\rm PE}(R(t'), t')\,{\rm d}t'\right], \tag{21}$$

where $\mathcal{I}(t) = \exp[-\int_0^t \mathcal{D}\,{\rm d}t']$. The first term governs the wind-driven evolution. The second is the photoevaporation correction convolved along the characteristic. Because the launch switch S modifies only the source term, it leaves the advective kernel $\mathcal{D}$ unbroken, allowing continuous superposition across the entire disc.

Equation (21) assumes the strict $\psi \gg 1$ limit. For general ψ, writing $\nu \propto R^\gamma$ with $\gamma = \frac{3}{2} - p$, self-similar mass balance demands an effective inner-disc slope ${\rm d}\ln\Sigma/{\rm d}\ln R = \xi(\psi,\lambda) - \gamma$. Here $\xi(\psi,\lambda)$ is the accreting root of:

$$2b^2 + (1+\psi)\,b - \xi_\infty\,\psi = 0, \qquad \xi_\infty \equiv \frac{1}{2(\lambda-1)}, \tag{22}$$

where $b \equiv a + \gamma$ (Tabone et al. 2022). This slope interpolates smoothly between the wind-dominated ($\xi \to \xi_\infty$) and purely viscous ($\xi \to 0$, giving $\Sigma \propto R^{-\gamma}$) limits.

The error in the closed-form exponent (equation 20) is exactly $\xi_\infty - \xi(\psi,\lambda)$: negligible at our fiducial $\psi \simeq 100$ (0.004), but 0.14 at $\psi = 1$. Sweeping our numerical integrator across $\psi \in [0.1, 10^4]$ at fixed $\alpha^0_{\rm DW}$ recovers this analytic $\xi(\psi,\lambda) - \gamma$ slope to within 0.09 dex.

One systematic bias persists even at $\psi \gg 1$. Dropping the viscous term turns the PDE from parabolic to hyperbolic. The full solver imposes boundary conditions at both $R_{\rm in}$ and $R_{\rm out}$, whereas the advective solution transports only from the outer boundary and leaves no freedom at the inner edge. Against the full two-term numerical integration, it therefore overestimates the surface density, and so $\dot{M}_{\rm acc}$, near the inner boundary by $\sim 10\%$.

3.4 Validity window, gap opening, and the dispersal cut-off

The analytic superposition (equation 21) is strictly valid only while photoevaporation does not reshape the advective characteristics. This requires the photoevaporative sink to stay negligible against net wind-driven advection, $[1 - S(\beta)]\dot{\Sigma}_{\rm PE} \ll (1-\xi)\Sigma v_{\rm DW}/R$. This bounds the closed form, not the model. The numerical integration carries the same equation through the reshaping and beyond, and the two coincide inside the bound. The window below is therefore where the analytic scalings may be read directly off the evolution.

This phase ends when a gap opens at $R_{\rm gap}$, defined by the balance:

$$[1 - S(\beta)]\,\dot{\Sigma}_{\rm PE}(R_{\rm gap}) = (1-\xi)\,\frac{\Sigma(R_{\rm gap})\,v_{\rm DW}(R_{\rm gap})}{R_{\rm gap}}. \tag{23}$$

The $(1-\xi)$ factor limits the resupply to the net advection remaining after local wind mass loss. Omitting it overstates the resupply and biases $R_{\rm gap}$ outward. The suppression factor $[1 - S(\beta)]$ further ensures that photoevaporation can carve a gap only where the magnetic wind has already shut down, so $R_{\rm gap}$ appears later than an unsuppressed comparison would predict. Its location when it does open, however, is largely unchanged. An analogous radius-dependent balance (local photoevaporative removal against local accretion-driven resupply) was derived independently for a purely viscous disc by Malanga et al. (2025), who minimise the ratio of the viscously supplied surface density to the photoevaporation rate to obtain both the gap radius and a criterion for inside-out versus outside-in dispersal. The wind-driven resupply term here plays the role their viscous solution does. Globally, the primordial phase follows the closed-form mass history of Tabone et al. (2022). For a magnetic field decaying with index ω_B, the disc mass and wind-ejection fraction are:

$$M_{\rm D}(t) = M_0\Big(1 - \frac{\omega_B t}{2t_{\rm acc,0}}\Big)^{1/\omega_B}, \quad f_M \equiv \frac{\dot{M}_{\rm w}}{\dot{M}_*} = \Big(\frac{R_{0,\rm T}}{R_{\rm in}}\Big)^{\xi} - 1. \tag{24}$$

The transition to the dispersal phase occurs at $t_{\rm max}$, defined when the wind-driven stellar accretion rate drops to match the integrated photoevaporation rate ($\dot{M}_*(t_{\rm max}) = \dot{M}_{\rm PE,int}$). This is the wind-driven analogue of the polynomial accretion cut-off of Ruden (2004) and Alexander & Armitage (2007).

The gap does not necessarily open at the peak of the photoevaporation profile ($R_{\rm peak} \approx 2.8$ AU). Its location is a diagnostic of the

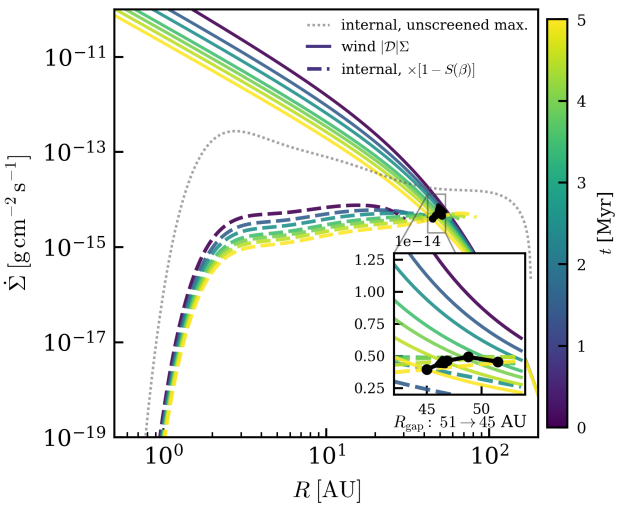

Figure 2. Mass-loss terms of equation (23), evaluated on real snapshots of the flux-retained run of Figure 3 (colour, t = 0–5 Myr). Solid: the wind-driven advective resupply. Dashed: the internal photoevaporation rate after the launch switch $[1 - S(\beta)]$, each curve cut off at that epoch's own screening radius $R_c(t)$, beyond which the profile is already suppressed. The fully unscreened profile is shown once (grey dotted) as the ceiling every other curve, at every epoch, lies below. Each intersection (dot) gives the predicted gap-opening radius $R_{\rm gap}$; the dots, joined in time order, trace how $R_{\rm gap}$ migrates inward, from 51 to 45 AU over 3.5–5.0 Myr, as $\dot{M}_{\rm acc}(t)$ declines.

mass-loss profile against the instantaneous accretion rate, not an imposed boundary condition. As Figure 2 shows, wind resupply can overwhelm mass loss well inside the disc, and the crossing point migrates inward over time as $\dot{M}_{\rm acc}(t)$ drops. On the flux-retained branch this is not a transition from the wind to photoevaporation through the launch switch. Since flux is retained while gas drains, β falls and $S(\beta)$ rises as the disc depletes, so $[1 - S(\beta)]$ suppresses the internal sink more over time. What drives the crossing instead is the retreat of the internal-PE screening radius $R_c(t)$ (Section 5.1): as the inner disc drains, $R_c(t)$ expands outward, exposing previously shadowed gas to direct irradiation faster than either the wind's decline or the strengthening launch switch can compensate.

To see how that crossing scales with stellar mass, we write the mass-loss profile in scaled form as $\dot{\Sigma}_{\rm PE}(R) = [\dot{M}_{\rm PE}/(2\pi R_s^2)]F(R/R_s)$. Where the wind is fully launched ($S \to 1$), equation (23) reduces to:

$$x^2 F(x) = (1-\xi)\,\frac{\dot{M}_{\rm acc}}{\dot{M}_{\rm PE}}, \qquad x \equiv \frac{R_{\rm gap}}{R_s}. \tag{25}$$

The radial scale R_s cancels, leaving the dimensionless crossing point dependent on M_* only through the ratio $\dot{M}_{\rm acc}/\dot{M}_{\rm PE}$. Comparing empirical accretion rates ($\dot{M}_{\rm acc} \propto M_*^{1.8}$; Manara et al. 2023) with standard photoevaporation scalings yields a weak dependence. The X-ray scaling of Owen et al. (2012) (using L_X from Güdel et al. 2007) scales as $M_*^{1.69}$, reducing the gap dependence to $\propto M_*^{0.11}$. The shallower hydrodynamic scaling of Picogna et al. (2021) ($\dot{M}_{\rm PE} \propto M_*^{1.0}$) yields $\propto M_*^{0.8}$. In both cases the gap opens well outside the mass-loss peak, which is a feature of the mass balance instead of an artefact of our 1 $M_\odot$ reference profile.

4 MAGNETIC FLUX TRANSPORT AND THE MAGNETOTHERMAL FRONT

The magnetothermal-to-thermal transition (Section 2.2) is not imposed at a fixed radius. It emerges from the recession of the magnetisation front as the inner disc loses the ability to sustain an MHD wind. We define that front from quantities the model already evolves instead of solving the flux-transport problem dynamically.

4.1 The magnetisation front and the launching threshold

The local launching condition is a midplane plasma beta below a threshold, $\beta(R,t) < \beta_{\rm crit}$, with $\beta_{\rm crit} \sim 10^4$–$10^5$. This is the net-vertical-field magnetisation at which non-ideal MHD simulations launch a dynamically significant magnetothermal wind and drive accretion at observed rates. A midplane $\beta_z \sim 10^5$ suppresses the MRI and sustains a laminar wind accreting at $\sim 10^{-8}\,{\rm M_\odot\,yr^{-1}}$, with the wind-driven rate scaling smoothly as $\dot{M}_{\rm acc} \propto \beta_z^{-1}$ (Bai & Stone 2013; Bai et al. 2016; Bai 2017; Lesur 2021). The condition therefore has no sharp cutoff (it weakens as a power law as β rises), and it is an intrinsic property of the field, set by magnetisation and non-ideal microphysics, not a comparison of mass-loss rates. Adopting a local field–column closure $B_z \propto \Sigma^q$, we obtain:

$$\beta(R,t) = \beta_0(R)\left[\frac{\Sigma(R,t)}{\Sigma_0(R)}\right]^{1-2q}, \tag{26}$$

where $\beta_0(R)$ is the initial midplane profile. We write $\beta \equiv \beta_P$ throughout, interchangeably, matching the notation of Sarafidou et al. (2024). The magnetothermal region is $\{R : \beta < \beta_{\rm crit}\}$, and its outer boundary $R_\beta(t)$ (the magnetothermal front) satisfies $\beta(R_\beta, t) = \beta_{\rm crit}$ and migrates as $\Sigma(R,t)$ evolves.

The threshold $\beta_{\rm crit}$ sets where a magnetised wind can be driven at all. That is distinct from whether the resulting wind is magnetically or thermally dominated, which depends jointly on the field strength and the X-ray luminosity. Sarafidou et al. (2024) mapped this parameter space with radiation–non-ideal-MHD models, finding magnetically dominated winds for $\log\beta_P \lesssim 3$ and predominantly thermal winds for $\log\beta_P \gtrsim 6$. These correspond to X-ray thresholds $\log(L_X/{\rm erg\,s^{-1}}) \approx 29.3$ and 30.8. For $\beta_P \gtrsim 10^5$ the total mass-loss rate converges to the purely photoevaporative value, whereas a strong field ($\log\beta_P \lesssim 4$) enhances it by roughly an order of magnitude. Early Ohmic-only simulations (Rodenkirch et al. 2020) placed that convergence at $\beta_P \gtrsim 10^7$. Ambipolar and Hall terms shift it to weaker fields, as the additional diffusion weakens the magnetic driving (Sarafidou et al. 2024, 2025).

These dominance boundaries lie at higher β than $\beta_{\rm crit}$ because they balance the wind against the photoevaporative floor ($\dot{M}_{\rm MHD}(\beta) \sim \dot{M}_{\rm PE}$) instead of establishing the fundamental launching capability. They therefore depend on the floor assumed: Sarafidou et al. (2024) used the Picogna et al. (2019) X-ray prescription, which sits an order of magnitude above the Sellek et al. (2024) rates adopted here. Because $\beta_{\rm cross} \propto \dot{M}_{\rm PE}^{-1/p_B}$, a lower floor shifts the magnetic/thermal boundary to higher β_P. Under the Sellek et al. (2024) rates, the magnetothermal wind dominates mass loss beyond the $\sim 10^5$–10^6 range Sarafidou et al. (2024) identify. The launching threshold itself is invariant (the field's capability to drive a wind does not depend on what a thermal wind would otherwise have removed), but the switch built on it is not equally immune. Through $[1 - S(\beta)]$, equation (17) partitions mass loss between the magnetothermal and thermal channels in equation (14), which is a dominance statement of the same kind as $\beta_{\rm cross}$. At $\beta = \beta_{\rm crit}$ half the photoevaporative rate is applied, rising to 91 per cent at $\beta = 10^5$. For the floor Sarafidou et al. (2024)

adopt, this tracks their transition closely. With the lower rates used here it concedes mass loss to the thermal channel sooner. We retain $\beta_{\rm crit} = 10^4$ because it is the launching threshold the simulations constrain, but flag the partition as an independent assumption sensitive to the photoevaporative floor.

4.2 The poloidal induction equation and the limits of a 1D solution

The secular evolution of this magnetisation is governed by the poloidal induction equation:

$$\frac{\partial B_z}{\partial t} = -\frac{1}{R}\frac{\partial}{\partial R}\left[R\left(v_\psi B_z - \eta_{\rm eff}\frac{\partial B_z}{\partial R}\right)\right], \tag{27}$$

where the behaviour is controlled by the large-scale magnetic Reynolds number $\mathcal{R}_m = |v_\psi|R/\eta_{\rm eff}$, with v_ψ the field-line drift speed and $\eta_{\rm eff} = \eta_{\rm turb} + \eta_{\rm AD}$. Writing the non-ideal physics as a single scalar $\eta_{\rm eff}$ omits the Hall term, which drifts the field with the electrons instead of dissipating it, with a sign set by the observationally unconstrained polarity of $\mathbf{B}_z \cdot \mathbf{\Omega}$. We do not integrate equation (27) dynamically, because a vertically averaged 1D model cannot capture the 3D transport mechanisms it would need. Appendix B shows what happens if one tries: integrated with a uniform-coefficient, wind-free, Hall-free reference model (Guilet & Ogilvie 2014), it redistributes flux outward. Lacking the meridional flows and Hall drift that drive inward advection in higher dimensions, the 1D diffusion operator smooths the field radially.

4.3 The self-limiting flux closure

Global 3D non-ideal calculations, however, report the net effect of poloidal flux transport to be inward advection and concentration (into rings and an inner zone), as opposed to outward diffusion with the draining gas, though the sign is not uniform at every radius or field polarity (Bai & Stone 2017; Suriano et al. 2018, 2019; Cui & Bai 2021; Lesur 2021). Because a 1D solve is biased toward outward diffusion and misses these 3D concentration mechanisms, we instead bracket the parameter space of equation (27) with two phenomenological extremes: a flux-retained branch ($\mathcal{R}_m \gg 1$) and a flux-loss branch ($\mathcal{R}_m \lesssim 1$).

The local closure index q carries this net trend, as a radius-resolved counterpart to the global field-decay index ω_B of Section 3. With the canonical wind-stress scaling $\alpha_{\rm DW} \propto \beta^{-p_B}$ (where $p_B \approx 1$ fits the ambipolar stratified simulations of Simon et al. 2013; Armitage et al. 2013), the advective flux yields $\alpha_{\rm DW} \propto \Sigma^{-p_B(1-2q)}$, so the global decay index is

$$\omega_B = p_B\,(1-2q), \qquad p_B \approx 1. \tag{28}$$

The sign of $1-2q$ governs the secular evolution. For any $q \le \frac{1}{2}$ the ratio $\beta(R,t)/\beta_0(R) = [\Sigma/\Sigma_0]^{1-2q}$ cannot rise as the disc drains. Gas depletion alone cannot demagnetise the plasma, and the closure is self-limiting. We adopt $q \le \frac{1}{2}$ as our fiducial configuration, with the specific value given in Table 1. In this regime, β falls during depletion, driving the same self-reinforcing accretion runaway described by Armitage et al. (2013) and Martel & Lesur (2022). This is strongest at the $q = 0$ endpoint ($\omega_B = 1$, strictly retained flux), where the field is frozen to the gas and their assumption is matched exactly. For $q > \frac{1}{2}$ (approaching flux freezing as $q \to 1$) the field decays fast enough for β to climb during draining. Because gas depletion is fastest in the inner disc, the wind is then quenched from the inside out: the transition radius R_β migrates to larger radii as the demagnetised region expands, and the disc is handed over to photoevaporation continuously on the local depletion timescale.

On the flux-loss branch the only route to an expanding demagnetised region is an independent reduction of B_z at fixed Σ by outward diffusion ($\mathcal{R}_m \lesssim 1$). In that diffusion-dominated limit equation (27) yields an effective global field-decay timescale $\tau_B \sim R_{\rm disc}^2/\eta_{\rm eff}$, making $\mathcal{R}_m \lesssim 1$ equivalent to $\tau_B \lesssim t_{\rm acc}$. The thin-disc value of $v_\psi/\eta_{\rm eff}$ is a long-standing open problem (Lubow et al. 1994; Guilet & Ogilvie 2012, 2014; Okuzumi et al. 2014; Bai & Stone 2017; Leung & Ogilvie 2019), so we treat $\mathcal{R}_m$ (equivalently τ_B) as the controlling unknown that brackets the two outcomes, a target for inference rather than a prediction. We refer to the resulting split in outcomes as a two-branch divide: these integrations probe only the two limits $\mathcal{R}_m \gg 1$ and $\mathcal{R}_m \lesssim 1$, not a continuous sweep of $\mathcal{R}_m$. This matches Armitage et al.'s conclusion that flux loss slower than mass accretion is the critical assumption behind two-timescale wind-driven dispersal.

4.4 The primordial-to-dispersal transition and its numerical closure

We define the primordial-to-dispersal transition operationally through the gap-opening condition (equation 23). This is the epoch and radius at which photoevaporation first overruns the local wind resupply, severing the disc and leaving the inner regions to drain onto the star without outer resupply. The front reaching the peak of the mass-loss profile, $R_\beta(t) \to R_{\rm peak}$, is a separate condition, marking when the most photoevaporative annuli become unmagnetised and any residual inner disc is swept on the terminal timescale. Which condition occurs first, and their radial separation, is a property of the particular integration. Both are moving boundaries derived from ($\mathcal{R}_m$, q, $\Sigma(R,t)$), unlike the fixed radii of classical thermal-wind models.

To follow this two-branch divide without integrating equation (27), we use a conservative finite-volume integration of the wind-dominated surface-density equation (Section 3), augmenting the algebraic closure (26) with the global exponential decay introduced in equation (2):

$$\beta(R,t) = \beta_0(R)\left[\frac{\Sigma(R,t)}{\Sigma_0(R)}\right]^{1-2q}\exp\left(\frac{t}{\tau_B}\right), \tag{29}$$

This parameterised decay is a proxy for outward flux diffusion. The flux-retained run takes $\mathcal{R}_m \gg 1$ ($\tau_B \to \infty$). The flux-loss run takes $\mathcal{R}_m \lesssim 1$ with $\tau_B = 0.5$ Myr, from the characteristic diffusion time $\tau_B \sim R_{\rm disc}^2/\eta_{\rm eff}$ for $\eta_{\rm eff} \sim 4\times10^{18}$ cm^2 s^{-1} (Guilet & Ogilvie 2014) evaluated at the outer grid edge $R_{\rm disc} \sim R_{\rm out} = 500$ AU. We evaluate it there rather than at the disc's characteristic mass scale ($R_{\rm c} \approx 30$ AU) because flux leaves the global budget permanently only once it diffuses out of the disc. Internal diffusion merely redistributes it radially.

What this costs should be stated plainly. A single global τ_B imposes a scalar approximation on a transport problem that is neither global nor scalar. It assumes $\eta_{\rm eff}$ applies uniformly across the disc, independent of local radial velocity $v_r(R)$ or gradients in the diffusivity, and it carries no representation of the Hall drift. Our own vertically averaged flux-transport calculation (Appendix B) shows why 1D approximations fail to reproduce the inside-out demagnetisation that the closure assumes. The two runs are therefore a phenomenological bracket on the limiting outcomes (establishing what follows if flux is retained or lost on a disc-lifetime timescale) and leave the transport mechanics to targeted 3D studies.

5 SECULAR EVOLUTION OF THE TWO FLUX-TRANSPORT BRANCHES

The closed forms of Sections 3–4 establish the model's scalings: the ejection index ξ shared between the launch and secular solutions (equation 20) and the stellar-mass dependence of the gap radius (equation 25), together with the result that depletion alone can never trigger dispersal under an algebraic $B_z(\Sigma)$ closure. Those are statements about every disc obeying the model, not evolutionary tracks for a particular one. Once the closure is allowed to feedback, the characteristics of Section 3.3 are straight only for spatially constant $\alpha_{\rm DW}$. The depletion factor $\Sigma_{\rm r}^{-(1-2q)}$ and the launch switch $S(\beta)$ both make $\alpha_{\rm DW}$ evolve with the solution instead. That feedback is what produces the two-branch divide.

We therefore integrate the governing equation numerically, verifying in Appendix C that the solver reproduces the analytic characteristics. The two branches identified in Section 4 differ solely in the imposed behaviour of the large-scale magnetic flux. We integrate them from identical initial conditions and with identical transport physics, so that every difference reported below is attributable to that one choice.

5.1 Numerical setup

5.1.1 Initial conditions and grid

We initialise a $1\,{\rm M}_\odot$ star and a $0.02\,{\rm M}_\odot$ disc on a one-dimensional grid spanning $R_{\rm in} = 0.5$ AU to $R_{\rm out} = 500$ AU, discretised into $N = 512$ logarithmically spaced cells with centres R_j, faces $R_{{\rm f},j}$ and cell area $A_j = 2\pi R_j\,\Delta R_j$. Outflow (zero-gradient) and zero-inflow boundary conditions are applied at the inner and outer edges respectively.

The initial gas surface density follows the viscous self-similar profile of Lynden-Bell & Pringle (1974),

$$\Sigma_0(R) \propto (R/R_{\rm c})^{-1}\exp(-R/R_{\rm c})\,, \tag{30}$$

with an exponential cutoff $R_{\rm c} = 30$ AU. We adopt this $\psi \to 0$ profile because it is the form discs are conventionally characterised with observationally, and a reasonable state after the initial gravito-turbulent phase. A wind-consistent alternative is in any case ill-posed for a radially varying lever arm λ (Section 2.1). We nonetheless verify in Appendix D that a wind-consistent initial profile at a higher accretion rate does not alter the two-branch divide described below.

5.1.2 Integration scheme and timestepping

The evolved variable is the cell mass $A_j\Sigma_j$, so mass is conserved by design. All transport (the wind flux, the viscous flux and the linear wind sink) is advanced by a single backward-Euler solve. Only the internal photoevaporative source is left explicit, being local and not stiff. The system is tridiagonal with positive diagonal and non-positive off-diagonals, an M-matrix. Its inverse is therefore non-negative, and the solve returns $\Sigma^{\rm new} > 0$ at any Δt, with no Courant condition.

The equation is nonetheless non-linear since the transport coefficients in equation (16) are functions of Σ. Each coefficient ($\alpha_{\rm DW}$, $S(\beta)$, the wind-base state, k_j and a_j) is evaluated at the old time level and held fixed across the solve, making the step linearised-implicit. Positivity is unconditional, since the M-matrix property follows from the sign structure of the assembled matrix alone. Accuracy is not. Lagging the coefficients renders the non-linearity first order in Δt, and it is that error, not stability, which the timestep coefficients bound.

The four dimensionless coefficients are the local sink rate, the advective rate, the viscous diagonal rate and the explicit photoevaporative removal, all evaluated only on cells retaining one per cent of their initial surface density and on their immediate neighbours. Integration stops once $\max_R \Sigma$ falls below $1\,{\rm g\,cm^{-2}}$.

Appendix C sets out the discretisation and the four timestep coefficients. It checks the scheme against the closed-form characteristics solution of Section 3.3, which it reproduces to under a quarter of a per cent over 1 Myr in the limit where that solution is exact. Appendix E1 additionally benchmarks the transport solver against the independent closed-form solutions of Tabone et al. (2022).

5.1.3 Viscosity, temperature and the initial field

A small turbulent viscosity $\alpha_{\rm SS} = 10^{-5}$ is included to represent residual hydrodynamic instabilities (e.g. the vertical shear instability). With $\alpha^0_{\rm DW} = 10^{-3}$ this gives a wind-to-viscous ratio $\psi = \alpha_{\rm DW}/\alpha_{\rm SS} \simeq 100 \gg 1$, so transport remains wind-dominated. The midplane temperature follows the passive-disc irradiation profile $T_{\rm mid} = 280\,(R/{\rm AU})^{-1/2}$ K with mean molecular weight $\mu = 2.34$, the same molecular value carried through the irradiated wind base (Section 2.2).

The initial midplane magnetisation is $\beta_0(R) = 30\,(R/{\rm AU})^{3/2}$, which crosses $\beta_{\rm crit} = 10^4$ at $R \approx 50$ AU. The wind is therefore launched out to $R_\beta(0) \approx 50$ AU, while the outer disc starts unmagnetised. The launch coefficient $\alpha_{\rm DW}$ includes the smooth cutoff $S(\beta)$ of equation (17), which weakens the wind as a power law instead of switching it off at a sharp boundary. Together with the depletion factor of equation (16) this gives $\alpha_{\rm DW} \propto \beta^{-1}$ inside the magnetothermal front, matching the $\dot{M}_{\rm acc} \propto \beta_z^{-1}$ scaling established by non-ideal-MHD simulations (Bai & Stone 2013; Bai et al. 2016; Bai 2017; Lesur 2021). Outside the front it gives $\alpha_{\rm DW} \propto \beta^{-2}$ instead, as discussed in Section 3. Beyond R_β the lever arm is taken from equation (13) rather than held at its launching value, and the two need not match: at $\beta_{\rm crit}$ that closure returns $\lambda = 3$ identically, while the derived value just inside R_β is whatever the Bai map gives there ($\lambda \approx 5$ at $t = 0$, falling below 3 later in the evolution), so the resulting step can run either way – visible as the discontinuity in Figure 3's dashed continuation beyond R_β. It is dynamically inert regardless, since it governs λ only where the launch switch is already suppressing the torque. Across the launching region the derived values ($\lambda \approx 4$–7, $\xi \approx 0.09$–0.16) straddle Bai et al.'s fiducial ($\lambda \simeq 5.2$, $\xi \simeq 0.12$), as befits a thermally assisted base.

5.1.4 The flux-closure index

The flux-closure index is fixed at $q = 0.3$ throughout. This is not a measured quantity, as the literature constrains the branch, not the value. The inward flux advection of Section 4 places the disc on the self-limiting $q \le \frac{1}{2}$ side, and within it $q = 0.3$ is a mid-range choice. By equation (28) it corresponds to a global decay index $\omega_B = p_B(1-2q) = 0.4$, inside the range $\omega_B = 0.25$–1 over which Tabone et al. (2022) construct their self-similar family. The integrator is validated against that same family (Appendix E1).

5.1.5 Photoevaporative sinks and shadowing

Internal photoevaporation is set by the X-ray-driven mass-loss profile of Sellek et al. (2024) (the column-integrated polynomial fit of their Table 3), scaled for a $1\,{\rm M}_\odot$ star with the same $L_X = 2\times10^{30}$ erg s^{-1} (0.5–5 keV) adopted in Section 2.2. It peaks at

$R_{\rm peak} \approx 2.8$ AU and carries a total rate $\approx 4 \times 10^{-9}\,{\rm M_\odot\,yr^{-1}}$. Appendix E2 benchmarks it, as implemented here, against Sellek et al.'s own published calculations. Following Picogna & Ercolano (2026), internal photoevaporation acts only on the directly-illuminated bulk disc. Beyond the co-moving cut-off radius $R_{\rm c}(t)$ the outer disc is screened by the inner disc (its scale height drops and the outer mid-plane no longer sees the ionising field), so $\dot{\Sigma}_{\rm PE}$ is smoothly suppressed there, by the factor $[1 + (R/R_{\rm c})^6]^{-1}$. We identify $R_{\rm c}(t)$ with the disc's current characteristic mass radius, the radius enclosing a fraction $1 - e^{-1} \approx 0.632$ of the instantaneous disc mass. For the initial profile (30) this returns the exponential-taper scale itself, $R_{\rm c}(0) = 30$ AU, so the initial condition is unchanged. It is, however, updated from $\Sigma(R, t)$ at every step, not held fixed, and is free to move in either direction as the disc evolves. It remains a proxy: a self-consistent treatment would track $H(R, t)/R$ and locate the shadowing front directly, which we list among the caveats.

5.2 The two-branch divide: front trajectories and accretion history

Figure 3 (bottom panels) tracks three radii:

(i) R_β, the magnetisation front of Section 4, where $\beta = \beta_{\rm crit}$;

(ii) $R_{\rm gap}$, the innermost radius at which the delivered photoevaporative rate overruns the wind's net advective resupply (equation 23);

(iii) $R_{\rm cav}$, the density-based inner-cavity edge, set by the $\Sigma/\Sigma_0 = 0.05$ threshold.

In the flux retained ($\mathcal{R}_m \gg 1$) branch, the magnetisation front R_β expands monotonically as the field concentrates and the wind strengthens. It grows from 47 AU to 77 AU by $t = 5$ Myr, and to ≈ 140 AU by 0.3 Myr before the branch's terminal collapse at $t \approx 6.25$ Myr. $R_{\rm gap}$ is first defined at $t = 3.19$ Myr at 55 AU, 3.1 Myr ahead of the collapse. It then migrates inward to 45 AU by $t \approx 5.2$ Myr as the accretion rate declines (see equation 23).

In the flux lost ($\mathcal{R}_m \lesssim 1$) branch, R_β instead recedes monotonically from 47 AU to a minimum of 3.6 AU at $t = 3.1$ Myr. $R_{\rm gap}$ already exceeds it the first instant both are defined ($t = 0.90$ Myr, $R_{\rm gap} = 37$ against $R_\beta = 16$ AU), 2.6 Myr ahead of that branch's collapse. Over the pre-collapse window the gap spans $R_{\rm gap} \approx 7$–37 AU, bounded above by the cut-off radius $R_{\rm c}(t)$ and lying well outside $R_{\rm peak}$. Although $\dot{\Sigma}_{\rm PE}$ peaks there, the inner disc is still wind-resupplied, so the balance is first lost further out, near the outer edge of the unscreened bulk disc (see Figure 2).

The gap's location relative to the front differs by branch. On the flux-retained branch it opens inside R_β, where the wind is still substantially coupled ($S(\beta) \approx 0.6$ at the crossing) and its resupply is a real competitor that photoevaporation only narrowly overtakes. On the flux-loss branch it opens outside the front, where the field has already receded to $S(\beta) \approx 0.2$ and the wind has correspondingly little resupply left to give. Flux retention therefore defers the gap and moves it inside the front rather than preventing it.

After the cavity edge overtakes the gap location ($t \approx 5.2$ Myr on the flux-retained branch, $t \approx 2.8$ Myr on the flux-lost one), they coincide to a single grid cell. From there only $R_{\rm cav}$ is a sensitive tracer.

The stellar accretion rate (Fig. 3, black dashed) distinguishes the branches by when it collapses: in both branches $\dot{M}_*$ declines smoothly from its initial value of $\sim 6.9 \times 10^{-9}\,{\rm M_\odot\,yr^{-1}}$, and then falls sharply to a numerically-floor-dominated residual once the innermost active accretion channel empties. Adopting $\dot{M}_* < 10^{-11}\,{\rm M_\odot\,yr^{-1}}$ as the criterion throughout, this happens at $t \approx 6.25$ Myr in the flux-retained branch and $t \approx 3.51$ Myr in the flux-loss one. The two branches differ by ≈ 2.7 Myr, far beyond the $\lesssim 2\%$ grid-resolution sensitivity of either collapse time (Appendix F), so the ordering is a robust feature of the two-branch divide. The collapse follows directly from a model assumption. The wind in this integration is switched off beyond R_β, so the screened outer disc cannot resupply the inner one once that reservoir is exhausted, and the disc drains to (numerical) completion instead of settling into the fed cavity steady state of Martel & Lesur (2022) and Sarafidou et al. (2025). Armitage et al. (2013) ran the equivalent experiment (the wind switched off outside an imposed radius, in their case a fixed 30 AU as opposed to a moving R_β) and did obtain a fed cavity, because in their model the outer disc remains viscous and supplies it. The difference here is the wind-dominated limit ($\psi \gg 1$, Section 5.1). There is no viscous reservoir left to do the feeding, so the same geometry gives terminal drainage instead of a quasi-steady cavity. Which of the two a real disc shows therefore depends on the residual turbulent stress in the screened outer disc, a quantity neither calculation constrains. Over a disc's lifetime, then, the branches are distinguished by the timing of this collapse and by the shape of $R_\beta(t)$ before either branch's own collapse (monotonically expanding versus monotonically receding), not by a persistently different asymptotic $\dot{M}_*$.

This two-branch divide makes a prediction that can be tested against resolved wind observations, because the two branches disagree about the state of the magnetothermal region at a given accretion rate rather than at a given time. Bajaj et al. (2026) analyse JWST/MIRI spectra of 72 inclined, mostly Class II discs and find that atomic jets and atomic–molecular winds of MHD origin dominate while a disc is accreting rapidly, whereas at lower accretion rates the jets weaken and the winds become predominantly atomic. Extended H_2 and the [O I] low-velocity component appear preferentially above $\dot{M}_* \sim 10^{-8.5}\,{\rm M_\odot\,yr^{-1}}$, and low-velocity [Ne II] emission preferentially below it. That ordering is the magnetothermal-to-thermal handover of this model, indexed by the same variable. Our two branches reach that accretion rate in comparable times but in opposite states. The flux-retained branch passes it at $t = 1.60$ Myr with R_β having expanded to 54 AU, while the flux-loss branch passes it at 1.22 Myr with R_β having receded to 11.6 AU, a factor of four inside its initial value. A population in which MHD wind tracers fade as accretion declines is therefore the flux-loss branch, not the flux-retained one.

Internal photoevaporation never reaches its full potential on the flux-loss branch. The magnetisation front recedes to a resolution-converged minimum of 3.61 AU, stopping 30 per cent short of $R_{\rm peak} = 2.766$ AU, so the radius where $\dot{\Sigma}_{\rm PE}$ is strongest stays wind-resupplied throughout the branch's life. The gap opens correspondingly far out, $R_{\rm gap} \approx 37$ AU ($\approx 13\,R_{\rm peak}$).

5.3 The wind base in the evolving disc

Figure 4 makes the wind-base decomposition of Section 2.2 quantitative.

The figure divides the disc by launching regime. A magnetocentrifugal wind is launched only inside R_β, where $S(\beta) > 1/2$ and the wind therefore carries more than half the mass loss (equation 17 with $\beta < \beta_{\rm crit}$). Inside it the base lies either below the irradiation front (a cold MHD wind, blue region) or at it (magnetothermal, green region). The switch closes smoothly, as opposed to abruptly, so a wind persists over $0.1 < S(\beta) < 1/2$ (the shaded region) while photoevaporation dominates it. Beyond that the outflow is purely thermal for $R < R_{\rm c}$ (pink region), and is suppressed beyond $R_{\rm c}$ (gray re-

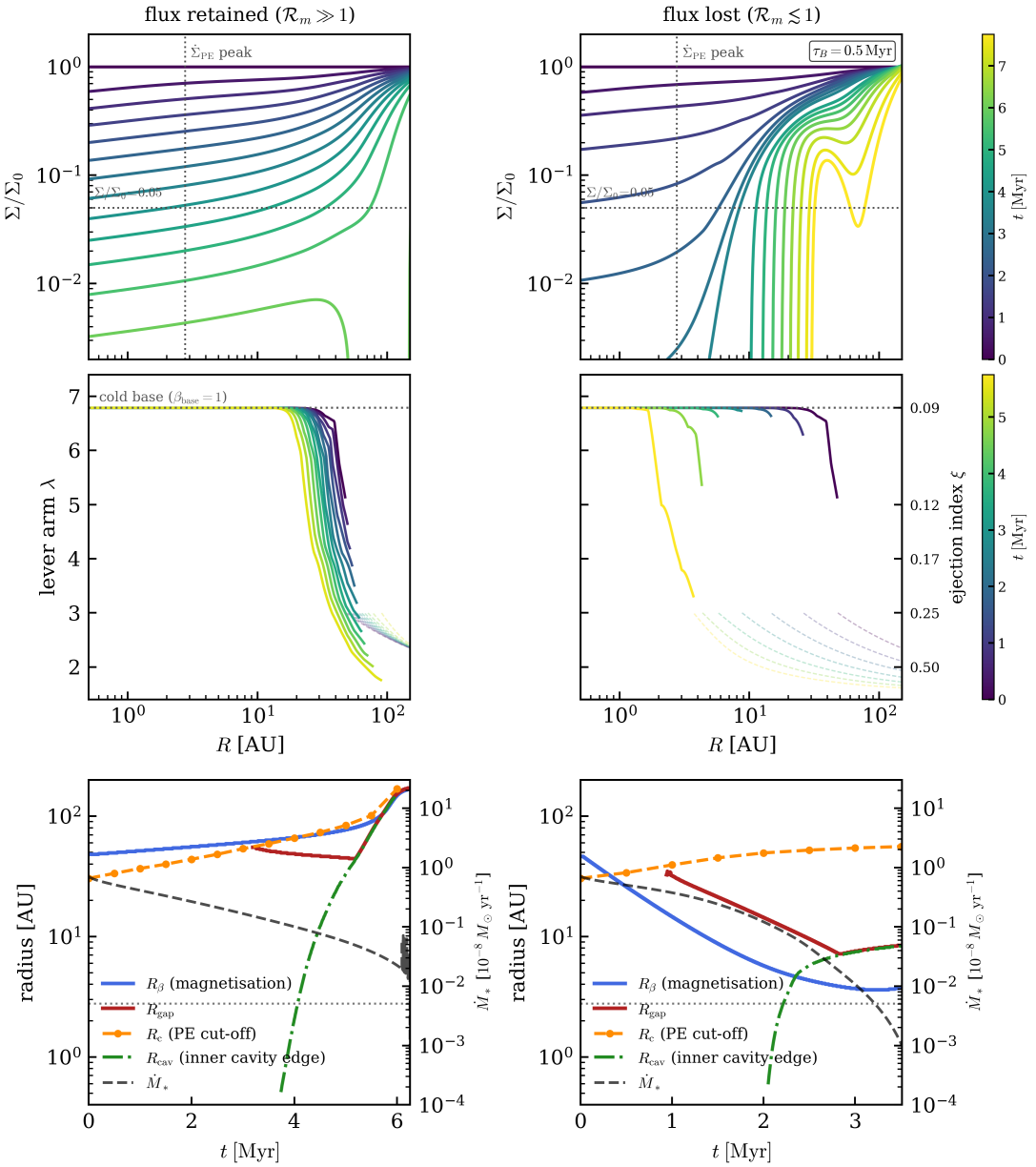

Figure 3. Coupled integration of the secular wind equation with the flux closure (26), under the fiducial Ξ–T wind-base prescription (Section 2), for a flux-retained run ($\mathcal{R}_m \gg 1$, left) and a flux-loss run ($\mathcal{R}_m \lesssim 1$, right). *Top:* surface density $\Sigma(R,t)/\Sigma_0$ evolution. *Middle:* derived lever arm $\lambda(R)$, solid over the launching region $S(\beta) > 1/2$ and continued faint and dashed beyond R_β, where $S(\beta) \leq 1/2$: the map still returns a value there, but it enters the torque multiplied by nothing and sources no wind, so it is a prescribed rather than a physically active quantity. The corresponding ejection index is $\xi = 1/[2(\lambda-1)]$. *Bottom:* front trajectories and $\dot{M}_*$, drawn up to and not beyond each branch's own accretion collapse. The diagnostics degenerate on floor-level gas immediately past it, and their resolution is only marginal in the final ~ 0.3 Myr before it (Appendix F1), so neither regime is shown. The evolution, and the distinction between the two gap measures, are described in Sections 3.4 and 5.2; convergence in Appendix F.

gion), where the inner disc's column screens the star. The wind-base temperature decides which threshold wins. $T_{\rm b}$ falls from $\approx$ 400 K at 0.5 AU and rejoins the mid-plane curve in the outer disc, which the isolated runs leave unheated ($T_{\rm b} = T_{\rm mid} = 28$ K at 100 AU; Section 2.2). A heated plateau of $\approx$ 100–130 K sits between the two fronts and moves inward with them. Beyond R_β that heated base matters only in the narrow transitional annulus with $0.1 < S(\beta) < 0.5$, where a sub-dominant residual wind torque survives. Elsewhere it adds no mass loss: the outflow is purely thermal, set by the photoevaporative sink term.

On the flux-loss branch the base crossover $z_{0,\rm th} = z_{0,\rm mag}$ separates the inner cold-MHD launch from the magnetothermal one. It sweeps inward as flux is lost, from 39.6 AU at $t = 0$ to 0.7 AU by $t = 3.5$ Myr, tracking the receding magnetisation front $R_\beta(t)$ (Section 5.2). The two are related but distinct radii ($z_{0,\rm th} = z_{0,\rm mag}$ versus $\beta = \beta_{\rm crit}$), and they do not recede together. A launch is magnetothermal only where the base has reached the irradiation front and the field still dominates the mass loss ($S(\beta) > 1/2$, i.e. $R < R_\beta$), so the magnetothermal region is the annulus between the two. At $t = 0$ the crossover lies inside R_β and that annulus is open. The front re-

cedes the faster of the two, however, and overtakes the crossover within 0.5 Myr. From then until $\approx$ 2.5 Myr the crossover sits outside R_β and the annulus is empty: the irradiated gas has fallen outside the launching region altogether and drives a purely thermal wind. It reopens over the final $\approx$ 1 Myr before collapse. By t = 3.5 Myr the crossover has receded to 0.55 AU, essentially the inner grid edge. The entire surviving launching region (0.55–3.76 AU) has therefore turned magnetothermal, the opposite of the branch's first two Myr. The driving mechanism varies sharply across that region: wind-dominated inside $\approx$ 1.5 AU ($\gtrsim$ 95 per cent of the local mass loss), crossing to photoevaporation-dominated ($\gtrsim$ 65 per cent) beyond $\approx$ 3 AU, with the 50/50 point falling close to $R_{\rm peak} \approx 2.8$ AU.

On the flux-retained branch the expanding front does not outrun the crossover, so that magnetothermal band is present from $t = 0$ and widens monotonically, from a factor 1.2 in radius to 3.1 by 5 Myr, with a base reaching $\approx$ 2.4 times the mid-plane temperature.

The magnetothermal launch that distinguishes this model from a superposed cold wind and thermal sink is largely a flux-retained-branch phenomenon by duration (on the flux-loss branch it is absent for most of the branch's life), but not by consequence. It reopens decisively in the final $\approx$ 1 Myr before collapse, and that is exactly where the branch clears. The results are insensitive to the choice of anchor in equation (9).

5.4 An inside-out disc clearing

Figure 3's top panels track the evolution of $\Sigma(R,t)/\Sigma_0$ on both branches until dispersal. Within the cut-off radius the dispersal proceeds through two channels acting in concert. The inner disc, which holds most of the mass, drains by wind-driven accretion, while internal photoevaporation removes the unscreened gas ($R \lesssim R_{\rm c}$), eventually opening a gap. Gas beyond $R_{\rm c}$ receives no internal mass loss at any given instant. The cut-off expands as the disc evolves, however, and material that was screened is progressively exposed.

On the flux-loss branch $R_{\rm c}$ grows from 31 AU at $t = 0$ to 62 AU by t = 5 Myr. The outer disc responds: Σ/Σ_0 at 80–120 AU falls to 70–92% of its initial value ($\approx$ 20 per cent of its mass). Internal photoevaporation is therefore not merely reshaping the inner disc. It is dispersing the whole of it, on a timescale set by how fast the screening lifts. The erosion accelerates accordingly. By t = 7.75 Myr, $R_{\rm c}$ has reached 106 AU, and the same annulus retains only 19 per cent of its mass. The region inside 100 AU (which held 96 per cent of the initial mass) is down to 3.1 per cent of what it started with, and the disc as a whole to 5.0 per cent. Internal photoevaporation alone therefore disperses this disc on a $\sim$ 10 Myr timescale, with no external irradiation required. We quote the sequence only to 7.75 Myr, where the run reaches the surface-density stopping criterion of Section 5.1, with no sign of stalling.

That clearing proceeds inside-out. The minimum of Σ/Σ_0 sits at the inner boundary throughout, and every depletion contour is anchored there and sweeps outward. The $\Sigma/\Sigma_0 = 0.5$ contour reaches 8.2 AU at t = 1 Myr, 25 AU at 2 Myr and 57 AU at 5 Myr. The direction is set by where the sinks act, not by the direction in which the screening front travels. The cut-off does move outward, but it only ever exposes gas to a photoevaporative profile that is itself centrally peaked, at $R_{\rm peak} \approx 2.8$ AU.

The mass-loss profile applied above is the one computed for an unbroken disc. Once a cavity has opened, the directly illuminated wall is eroded faster, and the profile is no longer the primordial one. That enhancement is calibrated and its consequences quantified in Appendix G.

On the flux-retained branch the outer disc is removed too, but almost entirely by the magnetothermal wind. There R_β expands, from 47 AU at $t = 0$ to 77 AU at 5 Myr, so the 80–120 AU band is progressively overtaken by the wind-active zone. Σ/Σ_0 there falls to 72% at t = 2.5 Myr and 31% at 5 Myr, reaching the numerical floor by 6 Myr, shortly before the branch's collapse. Internal photoevaporation accounts for 7% of the outer-disc removal by 5 Myr, and the expanding magnetothermal wind does the rest. This is so despite $R_{\rm c}$ expanding faster on this branch than on the flux-loss one, reaching 84 AU by 5 Myr against 62 AU: the cut-off does sweep the band, but the wind gets there first.

Neither branch clears from the outside in, and neither approaches a disc-wide, spatially uniform decline (i.e. the homologously depleting disc of Armitage et al. (2013); Wood et al. (2002)), which needs β_z held uniform in radius rather than tied to the locally evolving Σ as it is here. The two branches are not alike each other either, and the difference is observable. On both, the depleted region is anchored at the inner boundary and expands outwards. A cavity at the $\Sigma/\Sigma_0 < 0.05$ threshold opens at t = 2.05 Myr on the flux-loss branch and at 3.74 Myr on the flux-retained one, in each case at the innermost grid cell, and no detached gap forms at any epoch on either. What differs is how fast the cavity grows and what state the disc around it is in. The flux-loss cavity expands slowly (5.7 AU at 2.5 Myr, 8.3 at 3.5 and 13.5 at 5 Myr) while its outer disc is barely touched, Σ/Σ_0 at 80–120 AU still standing at 0.82 at 5 Myr. The flux-retained cavity opens more than a Myr later and then sweeps outward more than an order of magnitude faster (2.1 AU at 4 Myr, 33 at 5 and 151 at 6 Myr) into an outer disc that the expanding wind has already thinned to 0.30 of its initial surface density. The flux-loss branch therefore gives the conventional transition-disc morphology, a modest hole in an otherwise intact disc. The flux-retained branch instead depletes roughly evenly across the inner disc while R_β still holds the outer one, then, once dispersal kicks in, clears the remainder so rapidly that little is left outside by the time the hole is large.

The $\sim$ 10 Myr dispersal time of the flux-loss branch depends strongly on the screening radius, which is here diagnosed from the disc's characteristic mass radius, a function of Σ alone, while the shadow it stands for is set by the inner disc's aspect ratio $H(R,t)/R$, which the proxy never evaluates. What we can conclude is that internal photoevaporation can clear this disc unaided once the cut-off is free to move. The timescale on which it does so is not a calibrated prediction.

5.5 The lever arm of the evolving wind

The lever arm λ is the derived quantity that wind observations constrain directly. Each cell reads $\lambda = f(\beta_{\rm base})$ off the Bai et al. (2016) map (Section 2.1), with $\beta_{\rm base}$ set by the local field, the base height and the base temperature. Its evolution is therefore a prediction of the coupled system. It is shown in the middle panels of Figure 3 for the two branches. Because λ is meaningful only where a wind is actually launched, every statistic quoted below is restricted to the launching region $S(\beta) > 1/2$, i.e. $R < R_\beta$; Figure 3's middle panels additionally show its faint, dashed continuation beyond R_β, where the launch switch already suppresses the torque (Section 2.1).

Two features are important. The first is the plateau at $\lambda = 6.79$ ($\xi = 0.086$) that occupies the inner disc at every epoch on both branches. Where the base is set magnetically instead of thermally ($z_{0,\rm mag} < z_{0,\rm th}$, the cold-launch regime of Section 2.2), $z_{0,\rm mag}$ is defined as the height at which the local plasma beta reaches unity. This makes $\beta_{\rm base} = 1$ identically there, so λ takes the single value the map returns at that argument. The plateau is thus a direct consequence of the coupling criterion discussed in Section 2.2, and it

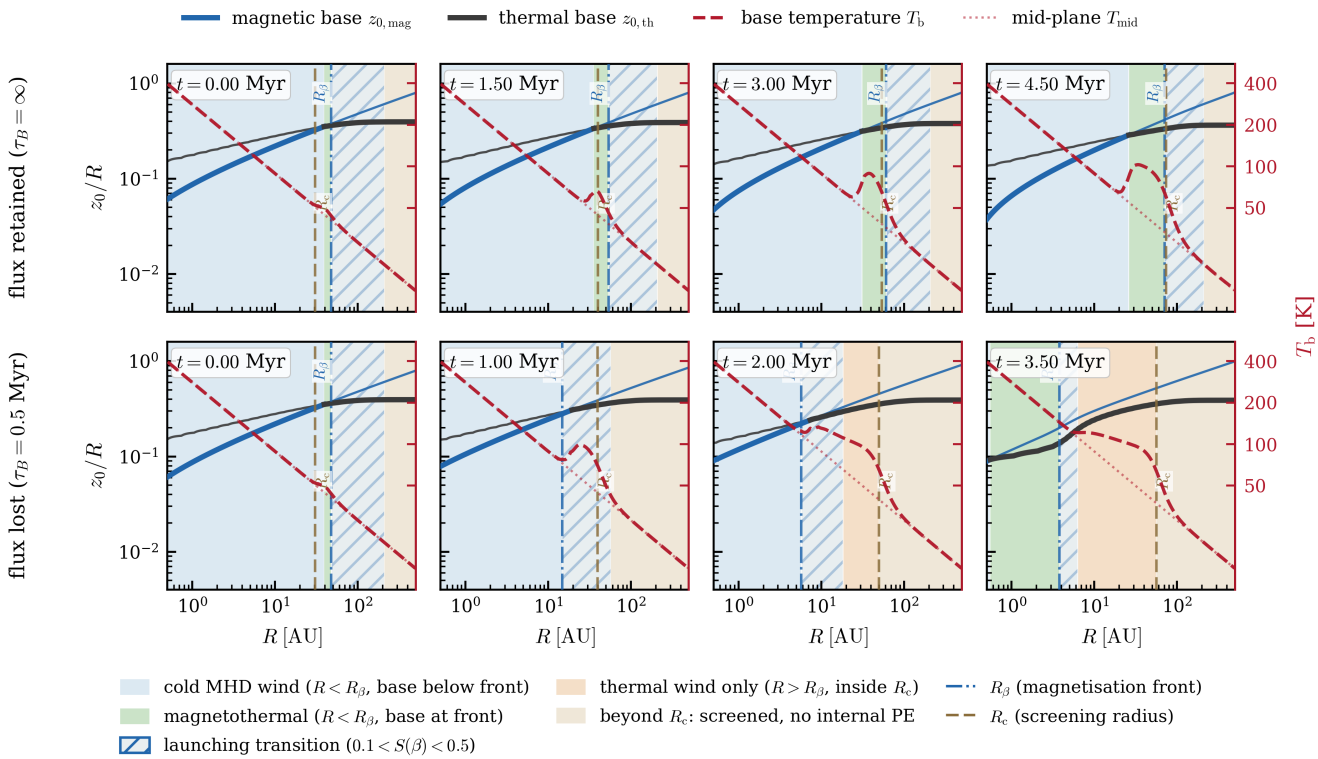

Figure 4. The wind-base launch mechanism on both branches. *Top row:* flux retained, R_β expanding. *Bottom row:* flux lost, R_β receding; epochs are labelled in each panel. Left axis: the competing base heights $z_{0,\mathrm{mag}}$ (blue) and $z_{0,\mathrm{th}}$ (dark), wind base z_0 = min of the two drawn thick. Right axis: the wind-base temperature T_b (red dashed) against the mid-plane T_mid (dotted). Shading gives the launching regime and the vertical lines the two radii bounding it, R_β and R_c (defined in Section 5.3). The shaded magnetothermal region is drawn in two levels: solid shading marks $S(\beta) > 1/2$, i.e. inside R_β, where the magnetothermal channel takes most of the mass loss. The hatched band marks $0.1 < S(\beta) \leq 1/2$, a weakly-launching shoulder outside R_β where the wind is sub-dominant and the complementary weight $[1 - S(\beta)]$ leaves the majority of the mass loss to the thermal channel.

inherits that criterion's uncertainty. A coupling height defined by an Elsasser number instead of by equipartition would move the plateau, though not the contrast between the branches. The second is that λ falls below the plateau only in the magnetothermal annulus, where the irradiation front lies below the magnetic base and the elevated $c_{\mathrm{s,w}}$ raises β_{base}. The lever arm is therefore a direct indicator of which launch regime each radius is in.

The branches separate in the spread of λ rather than in its typical value. On the flux-retained branch the magnetothermal shoulder is present from $t = 0$ and both widens and deepens. The minimum lever arm over the launching region falls from 5.2 to 1.5, the mass-weighted mean $\langle\lambda\rangle$ from 6.7 to 4.3 at 5 Myr, and the ejection index implied by that mean rises from $\xi = 0.088$ to 0.12. On the flux-loss branch λ is instead pinned at the cold plateau across essentially the whole launching region for the first 2 Myr (the median never leaves it, and $\langle\lambda\rangle$ stays within 2 per cent of its initial value), and then falls steeply to 4.8 over the final 0.7 Myr. That is the same statement as Section 5.3's, in the variable an observation can reach. The flux-loss branch launches an essentially cold, weakly loaded wind for most of its life and acquires a magnetothermal character only as it disperses, whereas the flux-retained branch carries a broad range of lever arms throughout.

Deriving the lever arm instead of prescribing it is not trivial, and it needs a fair baseline. A cold, weakly loaded launch corresponds to the model's own equipartition-base limit, $\lambda \approx 6.79$ at $\beta_{\mathrm{base}} = 1$ (Section 2.1). Repeating both named integrations with λ held fixed at that value, and altering nothing else, leaves the sustained accretion rate over 0.5–3 Myr unchanged on both branches. For most of each branch's mass-weighted life the derived λ sits on or near this same plateau (Figure 3). It does, however, delay the terminal collapse, by 5.8 per cent on the flux-retained branch and 1.6 per cent on the flux-lost one. The derived run alone departs from the plateau in its final approach to collapse, where the mass-weighted mean falls toward $\lambda \approx 2$, ejecting more mass than the fixed cold limit right when it matters most for the total budget.

Both branches straddle Bai et al. (2016)'s own fiducial $\lambda \simeq 5.2$, which the flux-retained mean crosses at $t \approx 3.6$ Myr and the flux-loss mean only in its final 0.3 Myr. An observationally inferred lever arm is weighted by the material that is actually flowing and emitting, whereas λ here is a local quantity at the wind base. The mapping between the two is not one-to-one, and the comparison should be read at the level of range and trend, not of a single number.

Martel & Lesur (2022) report $(\kappa, \lambda) = (2.2 \times 10^{-2}, 23)$ near the cavity and $(2.5, 3.2)$ in the outer disc, corresponding to $\beta_{\mathrm{BP}} \simeq 6.2$ and 15.7, respectively. As expected, the cold analytical relation holds tightly in the weakly loaded, magnetically dominated inner wind, but diverges by a factor of 3 for heavily loaded outer outflows.

The lever arms derived here can also be set against a direct measurement. Kim et al. (2026) resolve a rotating, nested outflow around the Class 0 protostar HOPS 358 and infer a dimensionless lever arm

$\lambda \simeq 2.3$, with the launching region constrained to 10–18 AU. Over those same radii our derived λ is ≈ 6.8, a factor of three larger. Three differences bear on the comparison. HOPS 358 is a deeply embedded Class 0 source while these calculations describe the Class II dispersal phase, at a different surface density and magnetisation. The observational value is inferred from outflow kinematics on scales well above the base, whereas ours is the local footpoint value. Finally, the two need not coincide even for one wind if the mass loading varies along the flow. The tension is nonetheless real, and it points in a definite direction: $\lambda \simeq 2.3$ implies a substantially heavier mass loading than the fiducial field strength selects. Equation (13) admits such values, since $\lambda \to 3/2$ as $\mu_w \to \infty$, so the formalism spans the measurement. What it does not do is select it at the adopted β. Since $\xi = 1/[2(\lambda - 1)]$, a lever arm of 2.3, compared with 6.8, would raise the wind mass loss per unit accretion by a factor of about four, so this is the sharpest observational test of the launch prescription currently available.

6 DISCUSSION

6.1 Relation to existing combined models

Numerical models that combine an MHD wind with photoevaporation already exist. Kunitomo et al. (2020) first evolved a one-dimensional disc under both a magnetically driven wind and a photoevaporative wind, finding that the former clears the inner disc early and the latter the outer disc late. Weder et al. (2023) built a population synthesis with magnetic braking, an MHD wind, and internal/external photoevaporation, including a semi-analytic prescription for the shielding of EUV photoevaporation by the MHD wind. Coleman et al. (2024) combine the Tabone et al. (2022) operator with Picogna et al. (2021)-type internal and FRIED v2 external photoevaporation, and state explicitly that they treat the MHD and photoevaporative winds "entirely separably" given the uncertainty in how the two interact. The AGE-PRO synthesis (Tabone et al. 2025) does not combine them at all: it contrasts two mutually exclusive populations, turbulence-driven accretion with Picogna et al. (2021) internal photoevaporation, against MHD disc wind evolution alone.

Where these models do include both, they add them as spatially separate processes. Weder et al. (2023) argue that the addition is a simplification, and that a cold MHD wind and photoevaporation are physically distinct in kind, so a single wind of an intermediate character should be expected instead. The present construction is an attempt at that wind. The launch is genuinely magnetothermal. The same irradiation sets the wind-base thermodynamics and drives the late-phase thermal wind, and the two are rationed by magnetisation instead of summed.

6.2 Relation to existing Green's-function solutions

Green's functions for the homogeneous magnetically-driven-wind operator have been derived independently. Shadmehri & Khajenabi (2024) obtained analytic time-dependent solutions, and a Green's-function solution in the same spirit has been presented in the tidal-disruption context (Tamilan 2026). The homogeneous kernel is therefore not new. The novel elements here are (i) the photoevaporation-sink convolution along the wind characteristics (equation 21); (ii) the coupling to a magnetothermal launch, so that $(\xi, \lambda, \alpha_{\rm DW})$ follow from a physically set base temperature instead of being free, together with the launch switch $S(\beta)$, which distributes one wind between its magnetothermal and thermal channels instead of summing two: the operator's own coefficient carries the magnetisation, and the thermal sink enters the convolution weighted by $[1 - S(\beta)]$; and (iii) the matched primordial-to-dispersal transition of Section 3.4, in which the gap-opening radius follows from the resupply balance of equation (23) instead of being identified with the classical gravitational radius.

6.3 Caveats

6.3.1 The isothermal launch proxy

The launch physics is compressed into a single isothermal base sound speed (equation 6). A rigorous treatment would enforce radiative equilibrium along the streamline, making the flow non-barotropic (e.g., the entropy-deposition model of Casse & Ferreira 2000b). We treat the Bai et al. (2016) ideal-MHD slow magnetosonic point not as a solver limit, but as an internal diagnostic of the magnetothermal-to-thermal boundary.

Applying the self-consistent Ξ–T prescription (Section 2) only where z_0 reaches the true irradiation front keeps the sustained-accretion lifetime within 4% of a strictly cold-base launch. Assuming full ionisation ($\mu = 0.65$) at that base would produce an artificial hot-base acceleration. We adopt molecular $\mu = 2.34$ across the internally irradiated base. While the blend parameter $f_{\rm hot}$ can explore hotter bases (Appendix A), the wind-base aspect ratio crosses $h \sim 0.3$ once $f_{\rm hot} \gtrsim 0.5$. Since the Tabone et al. (2022) operator is derived for a thin, subsonic disc, that sweep is meaningful only to $f_{\rm hot} \lesssim 0.25$.

6.3.2 Prescribed flux evolution and the missing cavity

The secular flux evolution remains unsolved, parametrised entirely by τ_B and the unconstrained field-divergence index $q_{\rm div}$. The assumed closure dictates the qualitative outcome: it selects the dispersal branch instead of deriving it. While Martel & Lesur (2022) showed that a flux-retaining cavity sustains accretion, our vertically integrated model does not reproduce it.

Our flux-retained branch does clear from the inside out, and does open a cavity (Section 5.4), but not an accreting one. The cavity appears only at $t = 3.74$ Myr, by which point $\dot{M}_*$ has already fallen to 1.2×10^{-9} from a plateau of $3.0 \times 10^{-9}\,{\rm M_\odot\,yr^{-1}}$, and the branch collapses at 6.25 Myr. The cavity is a late feature of a disc on its way out, not a long-lived accreting structure. The Tabone et al. (2022) operator imposes a subsonic radial velocity ceiling ($v_{\rm DW} \sim \alpha_{\rm DW} h c_s \ll c_s$) that cannot capture the transsonic radial flows expected in evacuated cavities. Reaching such flows would in any case require the inner disc to become strongly magnetised. With our adopted depletion scaling ($\beta \propto \Sigma^{1-2q}$ for $q = 0.3$), however, evacuating the cavity by three orders of magnitude lowers β by only one, so it never does before the whole disc collapses. Sustaining a steady transition-disc cavity requires a physical "conveyor" of poloidal flux inward, which our model lacks. Nor does Martel & Lesur (2022) establish that such a conveyor persists on secular timescales.

Whether the absent cavity is a defect of the model or of the parameters we adopt therefore has two answers. The subsonic ceiling follows from the form of the Tabone et al. (2022) operator, and no choice of $(\psi, q, \beta_0, \tau_B)$ removes it, so on that count the model cannot produce a transsonic cavity flow at any point in its parameter space. The magnetisation threshold, by contrast, is parametric. Because $\beta \propto \Sigma^{1-2q}$, the decade of β bought by three decades of evacuation at $q = 0.3$ becomes three decades at $q = 0$, and that endpoint is precisely where this model inherits the Armitage et al. (2013) and

Martel & Lesur (2022) accretion runaway. A cavity may well form elsewhere in (q, β_0, τ_B).

6.3.3 Internal photoevaporation and the screening proxy

Internal photoevaporation operates exclusively inside the screening radius $R_c(t)$ (Picogna & Ercolano 2026). We diagnose this cut-off from the mass radius, a proxy for the aspect ratio H/R. Its expansion as the disc drains is robust, but the timescale is not. The proxy depends only on Σ and ignores temperature, so lowering T_0 from 280 to 150 K flattens H/R by $\sim 25\%$ and leaves R_c unchanged. A physical shadow would shrink instead, accelerating outer-disc clearing. Tracking $H(R,t)/R$ dynamically is the required next step.

6.3.4 Vertical symmetry and multi-dimensional feedback

These calculations are vertically integrated and symmetric about the mid-plane by construction. Two results from multi-dimensional non-ideal MHD bear on that.

First, the sign of $\mathbf{B}_z \cdot \mathbf{\Omega}$ breaks the symmetry. Mori et al. (2025) find fast one-sided surface accretion, at $\sim$ 10 per cent of the Keplerian speed, and correspondingly asymmetric winds when the field is aligned with the disc angular momentum (the wind failing on the side that carries the accretion layer), while anti-aligned fields give more nearly symmetric outflows. Sarafidou et al. (2024) likewise find polarity-dependent structure in Hall-MHD. A vertically integrated treatment returns the average over the two surfaces and cannot represent that asymmetry. Since the polarity of any individual disc is observationally unconstrained (Section 4), the results here should be read as that average, as opposed to either surface.

Second, the wind reacts back on the irradiation front that defines its own base. Mori et al. (2025) find that the outflow enhances radiative heating by elevating that front. Our base height $z_{0,\mathrm{th}}$ is set by exactly this front, through the penetration column of equation (10), so the feedback acts directly on the quantity the base prescription computes, and is absent here. Relatedly, the thermal assistance in this model is evaluated locally at each footpoint, whereas in multi-dimensional calculations radiative transfer couples neighbouring streamlines (Gressel et al. 2020). The base-temperature sweep of Appendix A bounds the sensitivity to the base temperature itself, but not to a front whose height the wind has moved.

6.3.5 Scope of the closures

The result that $q \leq 1/2$ prevents demagnetisation assumes a fixed mid-plane temperature. Because $\beta \propto \Sigma^{1-2q} T^{1/2}$, an optically thinning cavity that heats up sharply could offset the Σ dependence and force demagnetisation even for $q \leq 1/2$. Separately, the closed-form characteristics (Section 3.3) assume $\psi \gg 1$. The numerical integrations retain the full operator, so this restricts only the analytic approximation, not the integrated results.

6.3.6 The unverified coupling criterion

The wind base is placed where the field reaches equipartition, $\beta_{\mathrm{couple}} = 1$, and the model never evaluates whether the gas there is in fact coupled to the field. No Elsasser number (ambipolar, Ohmic or Hall) is computed anywhere in the integration. The non-ideal terms enter only through this geometric proxy and through the prescribed τ_B. The proxy itself is well supported. Mori et al. (2025) find wind launching at $\beta \sim 1$ in global simulations carrying all three non-ideal terms with radiation transport, and equation (11) reproduces Bai & Stone's measured base height to 2.3 per cent (Section 2.2). What is assumed is not the criterion but its persistence: those calculations run for $\sim 10^2$–10^4 yr, and we apply their launching surface unchanged over 10^7. This has a sharper consequence than a missing diagnostic. Because $\beta_{\mathrm{couple}} = 1$ defines the magnetic base, wherever the base is magnetically set one has $\beta_{\mathrm{base}} = 1$ identically. The plateau $\lambda \simeq 6.8$ of Section 5.5 follows from that definition, not from the wind solution. The cold-launch lever arm is therefore a restatement of the coupling criterion, not an independent prediction of it. A coupling height set instead by $\Lambda_A \gtrsim 1$ would move the plateau, though, as shown there, not the contrast between the branches, which is carried by the magnetothermal annulus where β_{base} leaves unity. The requirement can be checked externally instead of internally. Sarafidou et al. (2025) measure $\Lambda_A \simeq$ 1–8 over 1–15 AU in a disc of this type, marginal inside $\sim$ 2 AU, and Mori et al. (2025) likewise launch from gas that is only marginally coupled, Am $\gtrsim$ 1. Both checks are borrowed, and both are taken at one epoch of a disc that is not evolving: the coupling of a draining disc is precisely what a non-ideal calculation would have to follow, and is the natural next constraint on this closure. The machinery for it exists. Delage et al. (2022) compute Ohmic and ambipolar diffusivities self-consistently from an ionisation network, with dust chemistry and irradiation heating, in a 1+1D vertically resolved disc. Steiner et al. (2025) carry the same class of calculation (thermal ionisation together with cosmic rays, stellar X-rays and radioactive decay, feeding Ohmic and ambipolar diffusivities) into the transport of a large-scale field, evolving the induction equation for the poloidal flux instead of prescribing it. Both calculations are steady-state. The first is MRI-driven, as opposed to wind-driven, and the second explicitly omits the toroidal field above the disc surface so as not to launch a wind, deferring outflows to a later paper in that series. The combination this model would need, a coupling height derived from a computed Elsasser number, carried through a secular wind-driven evolution, therefore does not appear to have been done. It is a concrete next step rather than an aspiration.

6.3.7 Absolute normalisation of the accretion rate

The fiducial disc mass (0.02 $M_\odot$) and stress ($\alpha_0 = 10^{-3}$) produce an early accretion rate ($\sim 6 \times 10^{-9}$ $M_\odot$ yr^{-1}) below typical Class II observations. However, since $\dot{M}_{\mathrm{acc}}$ scales linearly with $\alpha_0 M_{\mathrm{disc}}$, our core findings are dimensionless and invariant to this vertical offset (Appendix D). The scaling is bounded by the accretion timescale ($t_{\mathrm{acc}} = M_{\mathrm{disc}}/\dot{M}_*$), however: rates $\sim 10^{-6}$ $M_\odot$ yr^{-1} would drain the disc faster than flux-loss mechanisms can operate.

Similarly, the initial accretion rate scales linearly with the mid-plane normalisation $T_{\mathrm{mid},0}$, not with the base temperature, which Appendix A shows the launch to be insensitive to. Cooling the disc delays dispersal and widens the separation between the branches by roughly three quarters over 280 $\rightarrow$ 200 K, so a colder disc sharpens the two-branch divide instead of blurring it. However, these are upper bounds, as a realistic mid-plane temperature would evolve with the disc's optical depth and would lead to a flatter profile, accelerating the expansion of the screening radius and the clearing of the disc.

6.3.8 External photoevaporation and the imposed thermal structure

Every calculation presented here describes an isolated disc. The FUV field of the surrounding cluster enters neither as a mass-loss

sink beyond a truncation radius nor as a heating term at the outer wind base. That is not the situation of most discs, which form in regions where the ambient field is elevated by orders of magnitude and where external irradiation is known to truncate discs and shorten their lives (Haworth et al. 2018; Winter & Haworth 2022; Haworth et al. 2023). Whether a thermal wind then sweeps the residual disc is itself debated (Owen et al. 2013; Haworth et al. 2016), so we treat it as a possible, not a guaranteed, terminal channel. The extension is quasi-linear in Σ and therefore tractable within the same Green's-function framework. We defer it, with its numerical integration and its validation against the FRIED grid, to a companion paper (Picogna et al., in prep.).

Two things make it substantial. The FRIED rates are computed for unmagnetised, quasi-spherical outflows, so they cannot simply be added to a magnetothermal wind that is already removing the same gas. They have to be apportioned against it by the launch switch, exactly as the internal sink is. And beyond R_c an external field would set the base temperature while nothing in this treatment sets the base height there. Equations (9)–(11) locate z_0 from the stellar X-ray penetration column through a cold mid-plane structure, so photodissociation-region temperatures would be applied at an altitude derived for a shielded, colder layer. Locating the physical base under external irradiation needs an FUV penetration model that this vertically integrated treatment does not carry, and that is a prerequisite as opposed to a refinement.

The second is the mid-plane temperature. We impose $T_{\rm mid} = T_0(R/{\rm AU})^{-1/2}$ with $T_0 = 280$ K, held fixed in time. Only the wind-base temperature evolves. The consequences of that normalisation, and of freezing it, are bounded in the preceding subsection. What those bounds do not supply is an external check, and the two benchmarks available separate on exactly that point. Against Sellek et al. (2024), who likewise prescribe a temperature, the agreement is excellent (Appendix E2: 0.6 and 4.7 per cent in disc mass and accretion rate over 9 Myr). Against a calculation that instead solves the mid-plane temperature from irradiation, viscous heating and realistic opacities (Coleman 2021; Haworth et al. 2023), our disc drains viscously about twice as fast. In comparisons we have run but do not present here, the accretion channel removes 39 $M_{\rm J}$ over 4 Myr against that calculation's 19, and halving T_0 closes almost all of that particular gap.

It does not, however, rescue the comparison as a whole, and the way it fails is the reason we do not claim the external sink is validated. Repeating that benchmark at $T_0 = 140$ K across all three ambient fields raises every one of its twelve time-to-mass-threshold ratios, by factors of 1.4–1.7, and more than doubles the largest departure from the reference instead of reducing it ($\max|t_{\rm model}/t_{\rm ref} - 1|$ rises from 0.44 to 1.00). It also widens the spread among the three G_0 branches at every threshold. A residual that varies systematically with G_0 cannot be produced by a mid-plane temperature, which knows nothing about the ambient field. The discrepancy is therefore not a single thermal offset, and no uniform choice of T_0 removes it. Either the sink implementation carries a field-dependent error of its own (the mass-proportional partition, the treatment of cells falling outside the tabulated FRIED domain), or the reference's thermal structure is itself a function of G_0, which this model has no way to represent. Both readings point the same way: the external sink cannot be pronounced correct on the strength of this benchmark, and could not be even with the mid-plane temperature repaired.

These two limitations compound instead of adding. Any outer-disc sink competes for the same gas as accretion. A model that accretes too quickly therefore leaves such a sink less material and less time to act on, and would understate its importance. Adding external photoevaporation to the present thermal structure would therefore not settle how much the environment matters. The two have to be done together. That is the single clearest direction in which this model should next be extended.

6.4 Magnetically sustained photoevaporative gaps

A further implication concerns the wind inside a forming photoevaporative gap. Because the flux closure adopted here, $B_z \propto \Sigma^q$ with $q < 1/2$, lets the field decline more slowly than the gas, a gap carved by internal photoevaporation becomes progressively more magnetised as it drains. $\beta \propto (\Sigma/\Sigma_0)^{1-2q}$ falls with depletion, and $z_{0,\rm mag}$ drops below $z_{0,\rm th}$, so the base reverts to a magnetothermal launch within the gap. The residual gas can therefore keep driving a wind where a purely thermal treatment, in which the outflow loses its driving as the gap empties, instead finds it choking inside the gap (Weber et al. 2026).

Whether this operates while the gap is still forming (and so could sustain dispersal where a thermal-only wind stalls) turns out to depend on the branch, because two competing terms set β. Depletion lowers it as $(\Sigma/\Sigma_0)^{1-2q}$, while flux loss raises it as $\exp(t/\tau_B)$. When the flux is retained the first term acts alone, and the magnetothermal region expands into the draining disc at moderate depletion. Measured on the fiducial flux-retained run, it grows monotonically from 47 to 83 AU over 5 Myr, while the gas at 3 AU still holds 5 per cent of its initial surface density. On the flux-loss branch the same mechanism is defeated by the flux loss that defines the branch. The magnetothermal region instead recedes to ~ 3 AU by 3.5 Myr, and recovers only to ~ 6 AU by 5 Myr, in gas already depleted to $\Sigma/\Sigma_0 \sim 10^{-13}$, that is, once the gap is empty, as opposed to while it forms. A magnetically sustained gap is therefore a prediction for discs that keep their flux, not a route by which a demagnetising disc rescues its own dispersal.

Both statements are properties of the closure as much as of the model. The present vertically-integrated treatment does not resolve the wind's vertical structure, so whether a gap so magnetised actually launches is not settled here. A two-dimensional non-ideal MHD calculation with photoevaporative heating (as in Sarafidou et al. 2024, 2025) would test it directly.

7 CONCLUSIONS

We presented a two-phase model that couples a magnetothermal wind, launched from an irradiated base, to the secular evolution of a wind-dominated disc. The central result is structural. The standard flux-scaling closure $B_z \propto \Sigma^q$ (equation 26) is self-limiting: for $q \leq 1/2$, $\beta/\beta_0 = (\Sigma/\Sigma_0)^{1-2q}$ (equation 28) cannot rise as the disc drains. Gas depletion alone therefore cannot demagnetise a disc. Photoevaporation-dominated disc dispersal is not automatic; it requires an independent flux-transport dichotomy. Efficient flux loss ($\mathcal{R}_m \lesssim 1$) opens a photoevaporative gap. Flux retention ($\mathcal{R}_m \gg 1$) instead sustains accretion and defers dispersal. Integrating numerically the two branches we find:

(i) For a given initial magnetisation (Fig. 3; Section 5.2), the flux-retained branch's accretion rate collapses at $t \approx 6.25$ Myr; the flux-lost branch's collapses at $t \approx 3.51$ Myr. The split is a consequence of the magnetisation front R_β evolution, which expands from 47 to 140 AU on the flux-retained branch while it recedes to 3.6 AU on the flux-lost one.

(ii) $\mathcal{R}_m$ sets not only when the disc disperses, but in what state (Section 5.2). On the flux-retained branch, as the gas disperses it stops accreting. On the flux-lost branch the two decouple – accretion stops at $t \approx 3.51$ Myr, while the disc remains detectable for several Myr as a non-accreting transition disc. This is a testable population-level robust prediction of the $\mathcal{R}_m$ separation. However, the presence of an external FUV field might reduce the difference between the two branches (see Section 6.3).

(iii) Setting the wind base from stellar irradiation does not break the cold-launch assumption (equations 8 and 18; Appendix A). The base stays well below escape ($\varepsilon_b \leq 0.16$ pre-collapse). The torque is evaluated at the mid-plane sound speed (equation 18), so the base temperature does not affect the accretion rate directly. It reaches the launch only through the mass loading $\xi(\beta_{\rm base})$, whose effect is important only in the magnetothermal band, which is limited in time and space. This holds for an equipartition-set coupling height specifically ($\beta_{\rm base} = 1$). An ambipolar Elsasser-number criterion would not pin $\beta_{\rm base}$, and supplying one is the natural next step (Section 6.3).

(iv) The derived lever arm $\lambda = f(\beta_{\rm base})$ sits on a single plateau ($\lambda = 6.79$, $\xi = 0.086$) wherever the base is magnetically set, on both branches, for most of their lives (Fig. 3; Section 5.5). The branches separate in the spread of λ, not in its typical value. On the flux-retained branch the mass-weighted $\langle\lambda\rangle$ falls from 6.7 to 4.3 by 5 Myr as the magnetothermal shoulder widens and deepens. On the flux-lost branch it stays within 2 per cent of the plateau for the first 2 Myr and departs only in the final 0.7 Myr. Holding λ fixed at the plateau value leaves the sustained accretion rate unchanged on both branches, but delays the terminal collapse – 5.8 per cent on the flux-retained branch, 1.6 per cent on the flux-lost one. Measured against Kim et al. (2026)'s directly inferred $\lambda \simeq 2.3$ for HOPS 358, our launching-region value is a factor of three larger. Since $\xi = 1/[2(\lambda-1)]$, this is the sharpest quantitative test the launch prescription currently faces.

(v) Both branches clear inside-out, but by different mechanisms (Fig. 3, top panels; Section 5.4). Every depletion contour is anchored at the inner boundary and sweeps outward, because the sinks are stronger in the inner disc. On the flux-lost branch, internal photoevaporation alone disperses the disc down to 5 per cent of the initial mass by 7.75 Myr, with no external field required. The process self-accelerates when the cavity wall is directly irradiated by the central star, increasing by an order of magnitude the local mass-loss rate (Appendix G), and expanding the wall 3.2 times faster than the unperturbed profile would predict. On the flux-retained branch the outer disc is instead cleared almost entirely by the advance of the expanding magnetothermal wind (internal photoevaporation accounts for only 7 per cent of the removal by 5 Myr): the same front that strips the outer disc is the one whose collapse ends accretion, so inner and outer disc are exhausted within a fraction of a Myr of each other, compared with the prolonged transition phase the flux-lost branch shows (point 2). Clearing inside-out fixes where the front is anchored, not how far behind the outer disc lags. That lag is set separately by whichever process reaches the outer disc, and it is short here only because the wind itself is that process.

(vi) We do not recreate an accreting cavity (Section 5.2). Martel & Lesur (2022) and Sarafidou et al. (2025) associate the flux-retained regime with a long-lived, wind-fed cavity. Here, the cavity that does open forms at the innermost grid cell and never separates from the star. The wind has no viscous outer reservoir left to feed it once R_β has screened the outer disc. Armitage et al. (2013)'s imposed-boundary experiment differs in exactly this respect: its outer disc stays viscous, and does sustain a fed cavity. How a real disc behaves depends on the residual turbulent stress beyond R_β, a quantity neither calculation constrains.

Every result above holds at a single point in parameter space: one (q, β_0, τ_B), one stellar mass and X-ray luminosity, one disc mass and $\alpha_{\rm SS}/\alpha_{\rm DW}$. Several of these fixed parameters set the answer's normalisation instead of being passive choices: $M_{\rm d}$ and α_0 set the absolute accretion rate, $T_{\rm mid,0}$ additionally sets a timescale, and $\beta_{\rm crit}$ moves the initial front by a factor 4.6 per decade. What is guaranteed to survive a systematic sweep is the structural identity $\xi = 1/[2(\lambda - 1)]$, which forces the secular characteristics to recover the steady-wind profile $\Sigma \propto R^{\xi-1}$ (equation 20).

Three developments would move beyond this parameterised dichotomy. The first is solving the poloidal induction equation (equation 27) directly, to replace the imposed flux-decay timescale τ_B with an $\mathcal{R}_m$ set by disc microphysics. The second is external photoevaporation together with a solved mid-plane temperature; neither is present here, and the two interact, since a disc that accretes too fast leaves an environmental sink less mass to remove. The third is a population synthesis testing the $\mathcal{R}_m$ divide against the observed rarity and longevity ($\gtrsim 10^6$ yr) of mm-bright, high-accretion transition discs (Owen 2016). Such a synthesis would also confront Armitage et al. (2013)'s own demographic prediction – that the spread in disc lifetimes traces a spread in initial net flux.

ACKNOWLEDGEMENTS

This research was supported by the Excellence Cluster ORIGINS which is funded by the Deutsche Forschungsgemeinschaft (DFG, German Research Foundation) under Germany's Excellence Strategy - EXC-2094 - 390783311.

For the integrator and postprocessing scripts we adopted NUMPY (Harris et al. 2020), SCIPY (Virtanen et al. 2020) and MATPLOTLIB (Hunter 2007).

This work was carried out with the assistance of Claude Code (Sonnet 5). It was used to help draft and edit the text of this paper, to write and document the secular integrator and the figure-generation code. All physical assumptions, model choices, numerical prescriptions and interpretations are the authors' own; every quantity quoted in the text has been checked and the authors accept full responsibility for the content of this paper.

DATA AVAILABILITY

The secular integrator is available from the corresponding author upon reasonable request. The integrator output shown in Figure 3, together with the transition-disc radiation-hydrodynamic runs underlying Figure G1 (Appendix G), is archived at Zenodo `https://zenodo.org/records/22767933`.

REFERENCES

Alexander R. D., Armitage P. J., 2007, MNRAS, 375, 500
Alexander R. D., Clarke C. J., Pringle J. E., 2006, MNRAS, 369, 229
Anania R., et al., 2025, ApJ, 989, 8
Armitage P. J., Simon J. B., Martin R. G., 2013, ApJ, 778, L14
Bai X.-N., 2014, ApJ, 791, 137
Bai X.-N., 2017, ApJ, 845, 75
Bai X.-N., Stone J. M., 2013, ApJ, 769, 76
Bai X.-N., Stone J. M., 2017, ApJ, 836, 46
Bai X.-N., Ye J., Goodman J., Yuan F., 2016, ApJ, 818, 152

Bajaj N. S., et al., 2026, arXiv e-prints, p. arXiv:2607.21733
Béthune W., Lesur G., Ferreira J., 2017, A&A, 600, A75
Blandford R. D., Payne D. G., 1982, MNRAS, 199, 883
Casse F., Ferreira J., 2000a, A&A, 353, 1115
Casse F., Ferreira J., 2000b, A&A, 361, 1178
Clarke C. J., Gendrin A., Sotomayor M., 2001, MNRAS, 328, 485
Coleman G. A. L., 2021, MNRAS, 506, 3596
Coleman G. A. L., Mroueh J. K., Haworth T. J., 2024, MNRAS, 527, 7588
Cui C., Bai X.-N., 2021, MNRAS, 507, 1106
Delage T. N., Okuzumi S., Flock M., Pinilla P., Dzyurkevich N., 2022, A&A, 658, A97
Ercolano B., Clarke C. J., Drake J. J., 2009, ApJ, 699, 1639
Facchini S., Clarke C. J., Bisbas T. G., 2016, MNRAS, 457, 3593
Ferreira J., 1997, A&A, 319, 340
Gorti U., Hollenbach D., 2009, ApJ, 690, 1539
Gressel O., Turner N. J., Nelson R. P., McNally C. P., 2015, ApJ, 801, 84
Gressel O., Ramsey J. P., Brinch C., Nelson R. P., Turner N. J., Bruderer S., 2020, ApJ, 896, 126
Güdel M., et al., 2007, A&A, 468, 353
Guilet J., Ogilvie G. I., 2012, MNRAS, 424, 2097
Guilet J., Ogilvie G. I., 2014, MNRAS, 441, 852
Harris C. R., et al., 2020, Nature, 585, 357
Haworth T. J., Clarke C. J., Owen J. E., 2016, MNRAS, 457, 1905
Haworth T. J., Clarke C. J., Rahman W., Winter A. J., Facchini S., 2018, MNRAS, 481, 452
Haworth T. J., Coleman G. A. L., Qiao L., Sellek A. D., Askari K., 2023, MNRAS, 526, 4315
Hunter J. D., 2007, Computing in Science and Engineering, 9, 90
Kim C.-H., Lee J.-E., Johnstone D., Herczeg G. J., Lee C.-F., Francis L., Sheehan P. D., 2026, Nature Communications, 17, 2957
Komaki A., Nakatani R., Yoshida N., 2021, ApJ, 910, 51
Königl A., Salmeron R., 2011, in Garcia P. J. V., ed., , Physical Processes in Circumstellar Disks around Young Stars. pp 283–352, doi:10.48550/arXiv.1004.1875
Kunitomo M., Suzuki T. K., Inutsuka S.-i., 2020, MNRAS, 492, 3849
Lesur G. R. J., 2021, A&A, 650, A35
Leung P. K. C., Ogilvie G. I., 2019, MNRAS, 487, 5155
Lubow S. H., Papaloizou J. C. B., Pringle J. E., 1994, MNRAS, 267, 235
Lynden-Bell D., Pringle J. E., 1974, MNRAS, 168, 603
Malanga L. A., Rosotti G. P., Lodato G., Somigliana A., Manara C. F., Toci C., Testi L., 2025, A&A, 699, A292
Manara C. F., Ansdell M., Rosotti G. P., Hughes A. M., Armitage P. J., Lodato G., Williams J. P., 2023, in Inutsuka S., Aikawa Y., Muto T., Tomida K., Tamura M., eds, Astronomical Society of the Pacific Conference Series Vol. 534, Protostars and Planets VII. p. 539 (arXiv:2203.09930), doi:10.48550/arXiv.2203.09930
Martel É., Lesur G., 2022, A&A, 667, A17
Monsch K., Picogna G., Ercolano B., Kley W., 2021, A&A, 646, A169
Mori S., Bai X.-N., Tomida K., 2025, ApJ, 992, 85
Okuzumi S., Takeuchi T., Muto T., 2014, ApJ, 785, 127
Osterbrock D. E., Ferland G. J., 2006, Astrophysics of gaseous nebulae and active galactic nuclei, 2nd edn. University Science Books, Sausalito, CA
Owen J. E., 2016, Publ. Astron. Soc. Australia, 33, e005
Owen J. E., Ercolano B., Clarke C. J., Alexander R. D., 2010, MNRAS, 401, 1415
Owen J. E., Clarke C. J., Ercolano B., 2012, MNRAS, 422, 1880
Owen J. E., Hudoba de Badyn M., Clarke C. J., Robins L., 2013, MNRAS, 436, 1430
Pascucci I., Cabrit S., Edwards S., Gorti U., Gressel O., Suzuki T. K., 2023, in Inutsuka S., Aikawa Y., Muto T., Tomida K., Tamura M., eds, Astronomical Society of the Pacific Conference Series Vol. 534, Protostars and Planets VII. p. 567 (arXiv:2203.10068), doi:10.48550/arXiv.2203.10068
Perez-Becker D., Chiang E., 2011, ApJ, 735, 8
Picogna G., Ercolano B., 2026, MNRAS, 549, stag908
Picogna G., Ercolano B., Owen J. E., Weber M. L., 2019, MNRAS, 487, 691
Picogna G., Ercolano B., Espaillat C. C., 2021, MNRAS, 508, 3611
Rodenkirch P. J., Klahr H., Fendt C., Dullemond C. P., 2020, A&A, 633, A21
Ruden S. P., 2004, ApJ, 605, 880
Sarafidou E., Gressel O., Picogna G., Ercolano B., 2024, MNRAS, 530, 5131
Sarafidou E., Gressel O., Ercolano B., 2025, A&A, 696, A19
Sellek A. D., Grassi T., Picogna G., Rab C., Clarke C. J., Ercolano B., 2024, A&A, 690, A296
Shadmehri M., Khajenabi F., 2024, MNRAS, 528, 3294
Simon J. B., Bai X.-N., Armitage P. J., Stone J. M., Beckwith K., 2013, ApJ, 775, 73
Spruit H. C., 1996, in Wijers R. A. M. J., Davies M. B., Tout C. A., eds, NATO Advanced Study Institute (ASI) Series C Vol. 477, Evolutionary Processes in Binary Stars. pp 249–286
Spruit H. C., Uzdensky D. A., 2005, ApJ, 629, 960
Steiner D., Gehrig L., Güdel M., 2025, A&A, 703, A163
Suriano S. S., Li Z.-Y., Krasnopolsky R., Shang H., 2018, MNRAS, 477, 1239
Suriano S. S., Li Z.-Y., Krasnopolsky R., Suzuki T. K., Shang H., 2019, MNRAS, 484, 107
Suzuki T. K., Ogihara M., Morbidelli A., Crida A., Guillot T., 2016, A&A, 596, A74
Tabone B., Rosotti G. P., Cridland A. J., Armitage P. J., Lodato G., 2022, MNRAS, 512, 2290
Tabone B., et al., 2025, ApJ, 989, 7
Tamilan M., 2026, Progress of Theoretical and Experimental Physics, 2026, 023E02
Tarter C. B., Tucker W. H., Salpeter E. E., 1969, ApJ, 156, 943
Verner D. A., Ferland G. J., 1996, ApJS, 103, 467
Virtanen P., et al., 2020, Nature Methods, 17, 261
Wang L., Bai X.-N., Goodman J., 2019, ApJ, 874, 90
Wardle M., Koenigl A., 1993, ApJ, 410, 218
Weber E. J., Davis Jr. L., 1967, ApJ, 148, 217
Weber M. L., Ercolano B., Picogna G., 2026, MNRAS, 546, stag098
Weder J., Mordasini C., Emsenhuber A., 2023, A&A, 674, A165
Winter A. J., Haworth T. J., 2022, European Physical Journal Plus, 137, 1132
Wood K., Lada C. J., Bjorkman J. E., Kenyon S. J., Whitney B., Wolff M. J., 2002, ApJ, 567, 1183

APPENDIX A: WIND-BASE TEMPERATURE SENSITIVITY

The wind-base temperature, prescribed by our self-consistent Ξ–T prescription (Section 2), assumes a molecular mean weight of $\mu = 2.34$, and produces an effectively cold wind base.

As shown in Figure A1a, the fiducial run mirrors a strictly cold mid-plane launch. The peak accretion rates agree to better than one part in 10^3 (6.644 against $6.645 \times 10^{-9}\,\mathrm{M_\odot\,yr^{-1}}$), and the dispersal epoch to 0.03 per cent on the flux-loss branch (3.719 against 3.720 Myr). On the flux-retained branch the cold run reaches the 5 Myr sweep horizon without collapsing. Using the molecular μ lowers the base sound speed squared ($c^2_{\mathrm{s,w}}$) by a factor of 3.6 relative to a fully ionised gas, which would otherwise produce a hot-base acceleration.

The relation itself is the fit of Sellek et al. (2024, their eq. (14)),

$$\log_{10} T_{\mathrm{b}} = d + \frac{a-d}{\left[1 + (\log_{10}\Xi/c)^b\right]^m}, \tag{A1}$$

for which we adopt their Table 2 $T_{\mathrm{gas}} > T_{\mathrm{dust}}$ parameter set, $(a, b, c, d, m) = (1.1960, -2.8975, -0.1658, 4.0450, 1.0374 \times 10^4)$, instead of their all-cells set, since it is the irradiation-heated gas that sets the wind base.

This cold-base conclusion relies on three safeguards:

(i) Screening: The ionisation parameter Ξ is screened beyond the cut-off radius $R_{\mathrm{c}}(t)$, since Ξ otherwise assumes an unshadowed line of sight to the star that Picogna & Ercolano (2026) argue breaks down there.

(ii) Outer-disc reversion: Beyond $R_c(t)$, the base reverts to the cold mid-plane temperature.

(iii) Physical intercept: The heated base temperature is applied only where the magnetic base physically reaches the irradiation front ($z_0 = z_{0,\rm th}$, equation 10). Applying the hot temperature uniformly across the inner disc triggers an unphysical, rapid global draining.

The isolated runs are not given a corresponding ambient interstellar field, even though every disc sits in one. Applying that field's heating without a matching mass-loss sink would be inconsistent. The outer wind base in Section 5 should therefore be read as a lower bound.

We test this outcome against the assumed penetration column, lowering it from $N_{\rm b} = 10^{21}$ to 10^{20} cm^{-2}. A lower column shifts the irradiation front higher up, where lower density drives Ξ up: the median Ξ over the disc rises by a factor 7.2 and the base temperature by factors of 2–5 (Figure A1c). However, this elevated front is intercepted by the magnetic base over a much narrower radial extent: at $t = 0$ from $R > 67$ AU, compared with $R > 40$ AU. The two effects cancel almost perfectly out. The accretion rates over 0.5–3 Myr remain unchanged to three significant digits on both branches as shown in Figure A1a. The dispersal epochs do not match exactly. On the flux-loss branch the apparent +1.5 per cent shift is the criterion sensitivity of Section 5.2 as opposed to a physical delay. On the flux-retained branch, however, the hotter base delays collapse, from 5.45 to 6.80 Myr. Radial confinement of the heated region outweighs its higher temperature, so a warmer base over a narrower annulus is not a route back to hot-base acceleration. The cold-base outcome does not rest on the choice $N_{\rm b} = 10^{21}$ cm^{-2}.

Numerically, coupling the local surface density to the base temperature via the Sellek et al. (2024) Ξ–T fit requires two regularisations to maintain a well-posed secular integration. First, we evaluate Ξ at a smoothed $\log_{10}\Sigma$ (Gaussian, $\sigma \sim 5$ grid cells). The very large exponent m makes equation (A1) extremely steep near the transition, so grid-scale noise in Σ would otherwise be amplified into a spurious sharp front. Second, we apply the recombination-time relaxation (Section 2.2) to prevent a positive-feedback loop (hotter base $\rightarrow$ faster mass loss $\rightarrow$ lower Σ $\rightarrow$ hotter base) that would otherwise collapse the explicit timestep.

Finally, to bracket the base temperature independent of the Ξ–T relation, we use a simpler log-space blend between the cold mid-plane temperature $T_{\rm mid}$ and the capped escape temperature $T_{\rm esc}$ (equation 7) through a single parameter $f_{\rm hot} \in [0, 1]$, applied to the wind-torque sound speed and to the magnetic-coupling height $z_{0,\rm mag}$, but not to $z_{0,\rm th}$'s attenuation column, which describes gas the same photons have not yet heated. $f_{\rm hot} = 0$ recovers a strictly cold-base launch exactly. The sweep is nearly flat. Peak accretion is unchanged across its whole range, 6.645 to 6.652×10^{-9} M$_\odot$ yr^{-1} from $f_{\rm hot} = 0$ to 0.75. On the flux-loss branch, the dispersal epoch moves from 3.720 to 3.552 Myr, 4.5 per cent, over a sweep that takes the base from the cold mid-plane to three quarters of the way to the escape temperature.

The sweep is flat because the torque is evaluated consistently at the mid-plane sound speed, and the base temperature acts only through the mass loading $\xi(\beta_{\rm base})$. The residual 4.5 per cent is that surviving channel, integrated over the disc's life. These winds are effectively cold, and an hot base is not a route to rapid dispersal in this model. The flux-retained arm bounds rather than measures: all four of its runs reach the 5 Myr horizon without collapsing, so they establish only that no $f_{\rm hot} \leq 0.75$ brings that branch's collapse inside a window its fiducial (6.3 Myr under the same criterion) already sits outside. We integrate $f_{\rm hot} \in \{0, 0.25, 0.5, 0.75\}$, stopping each run at the first crossing of $\dot{M}_* < 10^{-12}$ M$_\odot$ yr^{-1}. This parameter space is in any case bounded by the thin-disc assumption of the Tabone et al. (2022) secular operator. As shown in Figure A1b, values of $f_{\rm hot} \geq 0.5$ drive the aspect ratio $h = c_{\rm s,w}/v_{\rm K}$ above 0.3 across most of the disc, so the operator is valid only for $f_{\rm hot} \lesssim 0.25$. That bound costs little since the response to $f_{\rm hot}$ is weak and it would not change the conclusion even if they could be trusted. Our self-consistent Ξ–T prescription sits at the cold end of the valid regime regardless.

APPENDIX B: A FIRST TEST OF THE POLOIDAL FLUX-TRANSPORT CLOSURE

In Section 4, we bypassed a direct solution of the induction equation (equation 27) in favour of the phenomenological τ_B proxy (equation 29). Here, we report an exploratory test of directly solving for flux transport using the vertically-averaged "simple reference model" of Guilet & Ogilvie (2014) (their eqs. 17–18), with field-line advection and diffusion rates $v_{\rm adv} = -1.5\nu/R$ and $v_{\rm diff} = \eta_{\rm eff}/H$.

Their model defines the local magnetic Reynolds number by comparing field-line advection to diffusion:

$$\mathcal{R}_m(R) = \frac{|v_{\rm adv}|}{v_{\rm diff}} = \frac{3}{2} P_{\rm B} \frac{H(R)}{R}, \tag{B1}$$

where $P_{\rm B} \equiv \nu/\eta_{\rm eff}$ is the turbulent magnetic Prandtl number and $\eta_{\rm eff} = \nu/P_{\rm B}$ is the diffusivity entering equation (27). Equation (B1) is not the same ratio as the large-scale $\mathcal{R}_m = |v_\psi|R/\eta_{\rm eff}$ of Section 4. The two differ by a factor H/R: the radial redistribution of B_z that sets $\tau_B \sim R^2_{\rm disc}/\eta_{\rm eff}$ occurs over R, whereas the competition between advection and diffusion that decides whether flux can be dragged inward at all is governed by how fast flux diffuses vertically out of a thin disc, over H (Lubow et al. 1994; Guilet & Ogilvie 2012). For $P_{\rm B} \sim 1$ the large-scale form would give $\mathcal{R}_m \sim 1.5$, marginally advection-dominated. Equation (B1), the form appropriate to the thin-disc problem, gives much smaller values: for this disc's aspect ratio ($H/R \simeq 0.028$ at the inner edge to 0.157 at the outer), $\mathcal{R}_m \sim 0.04$ –0.24 everywhere on the grid. It is the latter that the test in this appendix is measured against, using the order-unity threshold $\mathcal{R}_m^{\rm crit} \sim 1$ implied by the D parameter of Lubow et al. (1994) (their $\mathcal{R}_m = (2/3)/D$) and the turbulent magnetic Prandtl number $P_{\rm B} \sim 1$ that shearing-box MHD turbulence simulations and theoretical expectations both favour (Guilet & Ogilvie 2012).

Integrating equation (27) directly on this disc's actual, sharply radius-peaked initial field profile $B_{z,0}(R)$ does not reproduce the outside-in demagnetisation assumed by equation (29). The flux redistributes outward, demagnetising the inner disc while strengthening the field near $R \sim 50$ AU. This is not a numerical artefact (total flux is conserved to a few–20 per cent over the test window), and it is not a contradiction of the literature cited in Section 4 favouring inward flux concentration. It follows directly from Guilet & Ogilvie (2012)'s own analysis of equation (B1), since $\mathcal{R}_m \ll 1$ places the whole grid in the diffusion-dominated regime. Guilet & Ogilvie (2012) note explicitly that significant field bending, and hence inward concentration, instead requires an "unexpectedly large" Prandtl number, $P_{\rm B} \sim R/H \sim 6$–36 here, well above the shearing-box-turbulence value. They point instead to genuinely non-axisymmetric mechanisms (e.g. Spruit & Uzdensky 2005) as the more likely route to the concentration seen in global simulations.

Two ingredients absent from this reference model bear directly on that conclusion, and both act in the same direction:

(i) the wind torque: the reference model advects field lines solely via viscous inflow ($v_{\rm adv} = -1.5\nu/R$), whereas Leung & Ogilvie

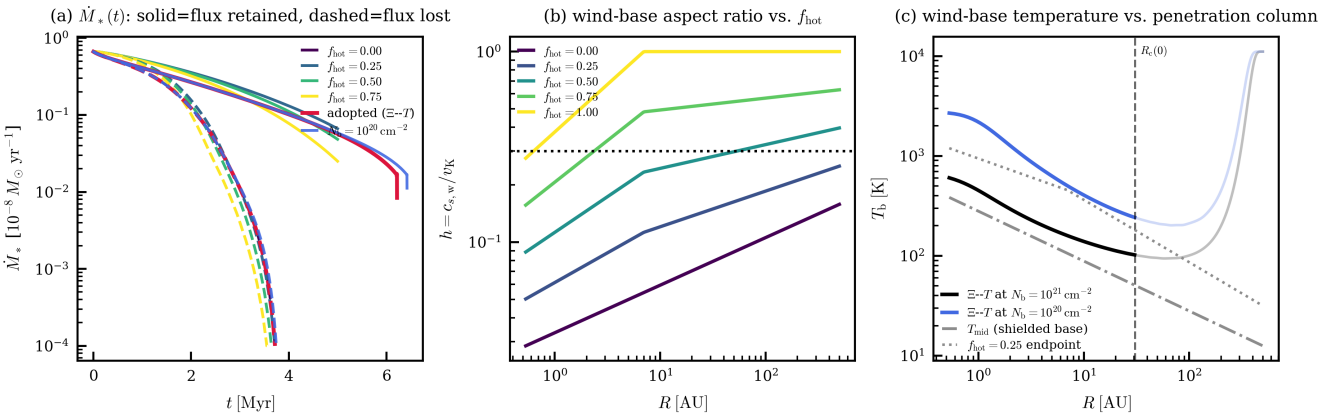

Figure A1. Wind-base temperature sensitivity. *(a):* stellar accretion rate $\dot{M}_*(t)$ for both branches (solid: flux retained, dashed: flux lost), swept over $f_{\rm hot} \in \{0, 0.25, 0.5, 0.75\}$ (colour), blending the wind-base sound speed between the cold mid-plane and capped escape-temperature endpoints. Each run stops at the first crossing of $\dot{M}_* < 10^{-12}\,{\rm M}_\odot\,{\rm yr}^{-1}$ or at $t = 5$ Myr. The adopted Ξ–T prescription (red) lies essentially on the cold $f_{\rm hot} = 0$ curve. Blue repeats the adopted prescription with the X-ray penetration column moved one decade, to $N_{\rm b} = 10^{20}\,{\rm cm}^{-2}$ (run to 7 Myr, since that is where the branches separate). Despite the much hotter base shown in *(c)*, the accretion histories are nearly indistinguishable. *(b):* the resulting wind-base aspect ratio $h(R) = c_{s,\rm w}/v_{\rm K}$, extended to the diagnostic-only $f_{\rm hot} = 1$ endpoint; the dotted line marks $h = 0.3$. *(c):* the wind-base temperature given by the Sellek et al. (2024) Ξ–T relation at the penetration column $N_{\rm b} = 10^{21}\,{\rm cm}^{-2}$ that defines the base (black), against the cold mid-plane and the $f_{\rm hot} = 0.25$ endpoint (grey). Blue repeats the Ξ–T relation at $N_{\rm b} = 10^{20}\,{\rm cm}^{-2}$: less penetration puts the front higher, where the density is lower and Ξ larger, and the base runs 2–5 times hotter, the input whose consequences panel *(a)* measures. The Ξ–T curves are faint beyond $R_{\rm c}(0)$, where it is not applied: its rise there is the outer taper's vanishing density inflating $\Xi = L_{\rm X}/(nr^2)$, not a predicted 10^4 K base. The jagged tails in (a) and the thresholds in (b) and (c) are discussed in the text.

(2019) find that it is a wind outflow that drives flux inward, with Hall drift significantly enhancing that inward transport in the positive-polarity case $\eta_H(\mathbf{B}_z \cdot \mathbf{\Omega}) > 0$, while Ohmic and ambipolar diffusivities drive transport outward. Coupled only to an outwardly inclined field, and with no wind, the Hall effect drives no flux transport at all. The advective side of equation (B1) is therefore the one term of the budget the reference model most clearly understates, and the values quoted above should be read as a lower bound on the true advection-to-diffusion ratio, not as an estimate of it.

(ii) the Hall effect: the model carries a single scalar diffusivity, $\eta_{\rm eff} = \eta_{\rm turb} + \eta_{\rm AD}$, so its transport is blind to field polarity, whereas Hall drift is not a diffusivity at all: it advects the field with the electron fluid, and its sense is set by the sign of $\mathbf{B}_z \cdot \mathbf{\Omega}$ (Bai 2014; Bai & Stone 2017; Leung & Ogilvie 2019).

Adding Hall drift is not a viable route to recovering inward concentration in the quasi-steady state. Bai & Stone (2017) find that for an aligned field the Hall effect rapidly drags flux inward at the mid-plane (the global manifestation of the Hall-shear instability), but that the resulting radially elongated field promotes rapid outward transport by ambipolar diffusion. The instability therefore saturates, and the quasi-steady rate is outward, comparable to the Hall-free case. For the anti-aligned polarity the Hall effect transports flux outward throughout, about twice as fast as the aligned case. On that evidence the outward redistribution found here is qualitatively consistent with the polarity-resolved simulations, not in tension with them, and the aligned polarity is the one that would favour inward transport, through the wind term, not through Hall drift acting alone.

The calculation closest to the configuration modelled in this paper is Sarafidou et al. (2024), which is polarity-resolved and carries internal X-ray heating. It is a 2D-axisymmetric non-ideal MHD calculation with Ohmic, Hall and ambipolar terms plus an X-ray temperature parametrisation, run at both orientations ($M_* = 0.7\,{\rm M}_\odot$, $|\beta_P| = 10^5$ at the mid-plane, and $L_X = 2 \times 10^{30}\,{\rm erg\,s}^{-1}$, the same X-ray luminosity adopted here). They confirm the polarity asymmetry in the sense described above: the two orientations differ by about two decades in laminar accretion rate ($\simeq 4 \times 10^{-9}$ versus $\simeq 2 \times 10^{-11}\,{\rm M}_\odot\,{\rm yr}^{-1}$), and the wind-launching radius moves from $\simeq 1$ au (aligned) to $\simeq 2.5$ au (anti-aligned). Their result that matters most here, however, is that the sign of the radial displacement is not fixed by the polarity alone. Within the same aligned run they recover the inward "pinch" only for $R < 5$ au, and find an outward "repulsion" of flux at $5 < R < 8$ au. They trace this to the sign of $J_\phi B_z$, and leave open whether the convex curvature is physical or an artefact of an initial condition with vanishing B_ϕ.

Either way, transport whose sign changes with radius within one calculation, at fixed polarity cannot be captured by a scalar $\mathcal{R}_m$, however that scalar is chosen. That limitation is sharper than the absence of a Hall term by itself, and applies equally to the closure of Section 4 and to the reference model tested here.

The net position is therefore weaker than a negative result. This test omits both terms that drive flux inward, so its outward redistribution is what their absence predicts. It does not adjudicate the phenomenological closure, and the sign of $\mathbf{B}_z \cdot \mathbf{\Omega}$ (unconstrained by observation, and fixed once per disc) remains a parameter of $\mathcal{R}_m$ that this work does not resolve. A test that could adjudicate the closure needs the wind torque in the flux budget, a polarity-resolved Hall term, and the vertically-resolved diffusivity structure Guilet & Ogilvie (2012) show is needed for realistic concentration even in an axisymmetric treatment. Until then, the uniform-coefficient, wind-free, Hall-free reference model tried here does not support replacing the phenomenological closure, which we therefore retain.

APPENDIX C: THE NUMERICAL SCHEME, AND ITS AGREEMENT WITH THE CLOSED FORM

The numerical integrations of Section 5 solve equation (14) directly, with the conservative finite-volume discretisation set out below. They do not evaluate the Green's function of equation (21). That closed form rests on a background, quasi-static treatment of the sink terms, and the point of integrating numerically is to avoid inheriting it. The two are therefore independent descriptions of the same equation, and this appendix checks the first against the second in the limit where the analytic solution is exact.

C1 Discretisation and timestep control

The evolved variable is the cell mass $A_j\Sigma_j$. The one term left explicit is the internal photoevaporative source, which is local, not stiff, and enters only through the right-hand side,

$$(A\Sigma)_j^{\rm exp} = A_j\Sigma_j - \Delta t\, A_j \dot{\Sigma}_{\rm PE,\,j}. \tag{C1}$$

Writing a_j for the advective coefficient at face j and V for the discrete viscous operator, the implicit update is

$$\Big[A_j(1+\Delta t\, k_j) - \Delta t\, a_j\Big]\Sigma_j^{\rm new} + \Delta t\, a_{j+1}\,\Sigma_{j+1}^{\rm new} - \Delta t\,(V\Sigma^{\rm new})_j = (A\Sigma)_j^{\rm exp}, \tag{C2}$$

with k_j the rate collecting the linear wind sink. The face value in the advective term is reconstructed by first-order donor-cell upwinding. Because the wind velocity is inward everywhere, the donor for face j is always cell j, so advection couples each cell only to its outer neighbour. The viscous operator couples both neighbours symmetrically, with non-positive off-diagonal weights. The system is therefore tridiagonal with a positive diagonal and non-positive off-diagonals (an M-matrix), and is solved directly in $O(N)$. That structure is what makes the solve positivity-preserving at any Δt.

The timestep is then set by accuracy alone. For a local sink $\mathrm{d}\Sigma/\mathrm{d}t = -k\Sigma$, backward Euler returns $1/(1+k\Delta t)$ against the exact $\mathrm{e}^{-k\Delta t}$, a local error $\sim (k\Delta t)^2/2$, so requiring one per cent per step gives $k\Delta t \le 0.14$. Three further dimensionless coefficients bound the advective rate $|a_j|/A_j$, the viscous diagonal rate, and the explicit photoevaporative removal $\dot{\Sigma}_{\rm PE}\Delta t/\Sigma$, at 0.03, 0.5 and 0.1 respectively. The first two are set by convergence against the independently implemented operator-split scheme, the third so that no cell loses more than a tenth of its surface density in one step. All four are evaluated only on cells still holding one per cent of their initial surface density, together with their immediate neighbours, for the reason given in Section 5.1.

C2 Agreement with the closed form

Section 3.3 solves the same equation in closed form in the wind-dominated limit. To enforce that limit we strip the transport down to pure wind-driven advection. The diffusive term is removed ($\alpha_{\rm SS} = 0$, i.e. $\psi \to \infty$), internal photoevaporation is switched off, $\alpha_{\rm DW}$ is held constant (which the depletion closure gives for $q = 1/2$), ξ is held constant, and the launch cutoff $S(\beta)$ is disabled (otherwise $\alpha_{\rm DW}$ acquires a radial dependence and the characteristics curve). The wind base is taken cold, so that $c_{\rm s}^2$ is the pure power law the derivation assumes. Each of these follows from the closed form itself, not from a preference about the physics. The characteristics are then straight, $R(t) = R_i - At$ with $A = \frac{3}{2}\alpha_{\rm DW}c_{\rm s}^2/v_{\rm K}$ constant, and the homogeneous solution along them is

$$\Sigma(R,t) = \Sigma_0(R+At)\left(\frac{R}{R+At}\right)^{\xi-1}. \tag{C3}$$

Equation (C3) is only the homogeneous kernel, so agreeing with it would test the advection operator and nothing else. The quantity of interest is the full equation (21), whose second term convolves the photoevaporative source along the same characteristics. Along $R(t') = R_i - At'$ the integrating factor closes analytically, $\mathcal{I}(t') = (R(t')/R_i)^{1-\xi}$, so equation (21) can be evaluated by quadrature against the same $\dot{\Sigma}_{\rm PE}$ and the same co-moving cut-off $R_{\rm c}(t)$ the integration uses. We therefore run the comparison twice: once with the source off, against equation (C3), and once with internal photoevaporation active, against equation (21). The second run uses the additive combination in place of the fiducial suppressed one, because $\beta_{\rm crit} \to \infty$ sends $S \to 1$ and would switch the suppressed source off entirely, leaving nothing to test. That is the one respect in which the check departs from the production configuration.

Figure C1 shows the result for $A = 10.49$ AU Myr^{-1} and $\xi = 0.25$. Over 459 cells spanning 1–500 AU the numerical solution reproduces the closed form to a median $|\Delta \log_{10}\Sigma|$ below 10^{-4} dex at $t = 0$, rising only to 0.0010 dex, under a quarter of a per cent, after 1 Myr, with a maximum of 0.034 dex. The two runs agree with their respective analytic solutions equally well. The residual is not distributed uniformly, and neither is the term being tested. Inside $\approx$ 30 AU, where the source acts, the photoevaporative correction grows to 5.6 per cent of Σ by 1 Myr (0.025 dex, dashed in the right-hand panel) while the residual there is 0.0012 dex. The convolution term is therefore recovered to about five per cent of its own magnitude. Outside $\approx$ 50 AU the source has vanished and the residual is instead set by advection, accumulating outward because the characteristics import material from ever larger $R_i = R + At$, where the initial profile is falling exponentially. That outer residual is a property of any finite-mass disc, not of the scheme, and it bounds the comparison, not the integration.

APPENDIX D: A HIGH-ACCRETION RUN FROM A WIND-CONSISTENT INITIAL CONDITION

Two objections can be raised at once against the fiducial integrations of Section 5. The first is that their absolute accretion rate ($\sim 6\times10^{-9}\,\mathrm{M_\odot\,yr^{-1}}$) sits below the bulk of young Class II accretors (Section 6.3). The second is that they start from the viscous Lynden-Bell & Pringle (1974) profile $\Sigma_0 \propto R^{-1}\exp(-R/R_{\rm c})$, which is the $\psi \to 0$ initial condition, in a model whose transport is wind-dominated. To confirm the results are not artefacts of either choice, we answer both with a single pair of runs: both branches restarted from the wind self-similar profile of Tabone et al. (2022), $\Sigma_0 \propto (R/R_{\rm c})^{\xi-1}\exp(-R/R_{\rm c})$, normalised to the high end of the observed Class II range.

Only five aspects of the setup differ from the fiducial run:

(i) Ejection index: unlike the fiducial's $\Sigma_0 \propto R^{-1}$ profile, which does not depend on ξ, the wind-consistent profile here does. It is then initially set to the same plateau value as the fiducial run: $\xi = 0.0864$ ($\lambda = 6.79$).

(ii) Disc mass: raised to 0.1 $\mathrm{M_\odot}$, which gravitational stability caps ($Q_{\rm min} = 3.96$ at 0.1 $\mathrm{M_\odot}$; $Q_{\rm min} = 2.02$, marginal, at 0.15 $\mathrm{M_\odot}$).

(iii) Transport stress: $\alpha_{\rm DW}^0 = 5\times10^{-3}$, calibrated by short integrations on the actual profile instead of scaled analytically. With the disc mass above this gives $\dot{M}_*(0) = 1.25\times10^{-7}\,\mathrm{M_\odot\,yr^{-1}}$.

(iv) Preserved magnetisation: $\beta_0(1\,\mathrm{AU}) = 30$ is held, so the launching state is preserved: $R_\beta(0) = 47.2$ AU, against the fiducial's 47.16 AU.

(v) Time scaling: τ_B and $t_{\rm end}$ are rescaled by the ratio of accretion timescales, $f = t_{\rm acc}/t_{\rm acc}^{\rm fid} = 0.954/3.241 = 0.294$, giving

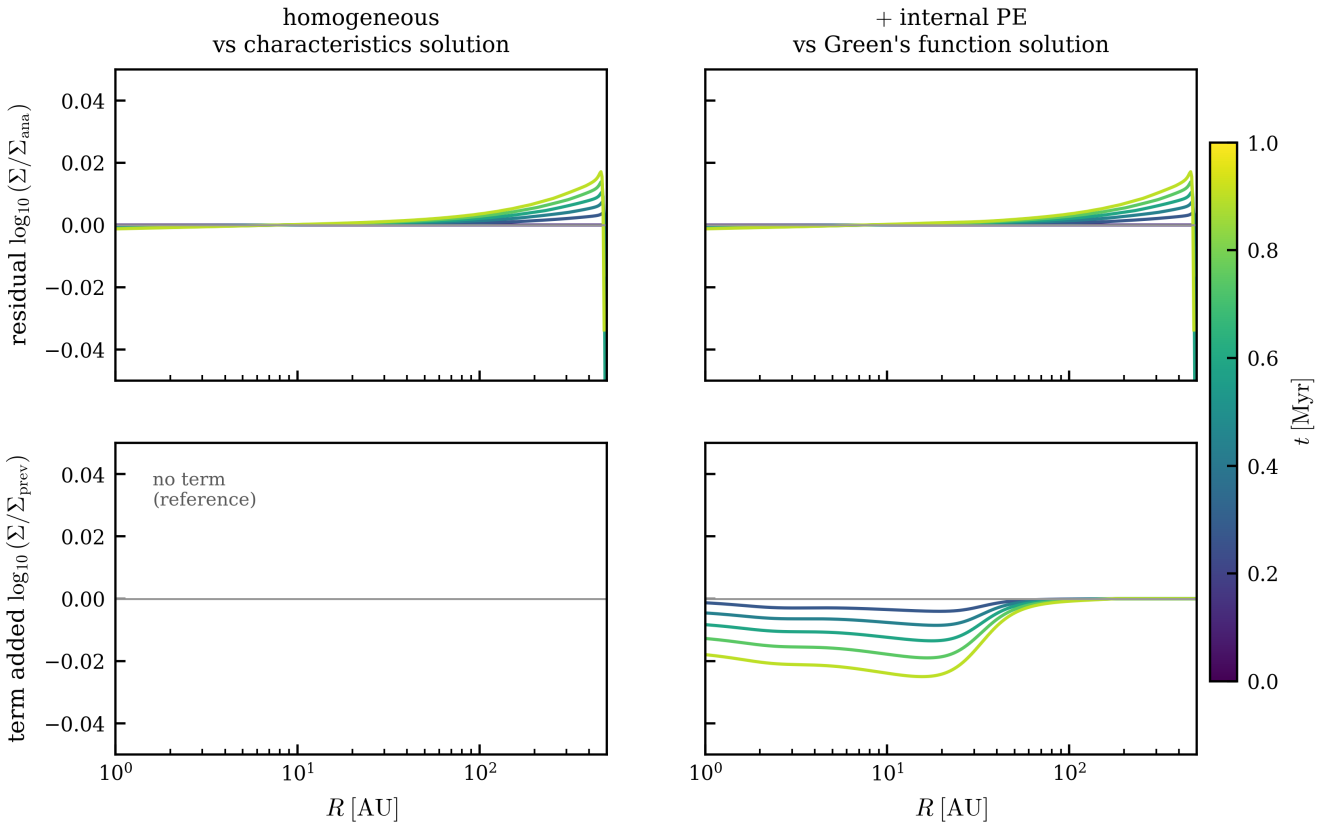

Figure C1. The transport solver against both closed forms, in the limit where they are exact, plotted against radius R and coloured by time from $t = 0$ to 1 Myr (bar at right). *Columns:* the homogeneous characteristics solution (equation C3) and the Green's function with internal photoevaporation (equation 21). *Top:* the residual $\log_{10}(\Sigma/\Sigma_{\rm analytic})$ against each. *Bottom:* the size of the term that column adds, $\log_{10}(\Sigma/\Sigma_{\rm prev})$, on a symmetric-log scale. Configuration and interpretation in Appendix C.

$\tau_B = 0.15$ Myr and the same per-branch horizons the fiducial uses, $t_{\rm end} = 3.0$ and 1.5 Myr for the flux-retained and flux-loss branches. That rescaling is not trivial. The two-branch divide is governed by $\tau_B/t_{\rm acc}$, not by τ_B alone (it asks whether flux is lost within a disc lifetime), so holding $\tau_B = 0.5$ Myr while $t_{\rm acc}$ shortens by 3.4 would change the regime rather than the timescale. With the rescaling, $\tau_B/t_{\rm acc}$ and $t_{\rm end}/t_{\rm acc}$ match the fiducial's to 1.9 per cent.

Maximize the initial accretion rate

The accretion rate cannot be raised freely, and the obstruction is not numerical. For the irradiated profile $c_{\rm s}^2 \propto R^{-1/2}$ the wind-driven drift $v_{\rm DW} = \frac{3}{2}\alpha_{\rm DW} c_{\rm s}^2/v_{\rm K}$ is radius-independent, so for $\Sigma \propto R^{-1}$ the accretion rate is too, and the accretion timescale is

$$t_{\rm acc} \equiv \frac{M_{\rm disc}}{\dot{M}_*} \approx 2.9\ {\rm Myr}\left(\frac{10^{-3}}{\alpha^0_{\rm DW}}\right)\left(\frac{R_{\rm c}}{30\ {\rm AU}}\right). \tag{D1}$$

in which $M_{\rm disc}$ cancels: raising the disc mass raises the reservoir and the rate in exact proportion, so it cannot repair the mismatch. Fixing $\dot{M}_*$ and $R_{\rm c}$ therefore fixes $t_{\rm acc} = M_{\rm disc}/\dot{M}_*$ (equation D1), and the only remaining freedom, $M_{\rm disc}$, is capped near 0.1 $M_\odot$ by gravitational stability. Demanding $\dot{M}_* \sim 10^{-6}\ M_\odot\ {\rm yr}^{-1}$ therefore forces $t_{\rm acc} \lesssim 0.1$ Myr. The disc empties before τ_B can act at all, so the model's central two-branch divide cannot be evaluated at that rate. A 5 Myr run at $10^{-6}\ M_\odot\ {\rm yr}^{-1}$ would need $M_{\rm disc} \approx 5\ M_\odot$.

The two-branch divide survives

As shown in Figure D1, the two-branch divide survives intact at 17 times the fiducial accretion rate and from a different initial profile. The magnetisation front expands on flux retention (R_β : 47.2 → 87.7 AU before collapse) and recedes on flux loss (47.2 → 3.0 AU). The photoevaporative gap opens on both (1.47 Myr at 97.7 AU, and 0.50 Myr at 52.5 AU). Finally, the flux-retained branch outlives the flux-loss one, collapsing at 1.92 Myr against 1.37 Myr, each comfortably inside its own horizon. Every qualitative element of Section 5.2 therefore reappears at an accretion rate an order of magnitude higher and from a wind-consistent instead of a viscous initial profile.

The sizes of these intervals are a different matter, and we do not claim they transfer. Expressed in units of each run's own $t_{\rm acc}$, the flux-retained collapse does reproduce the fiducial's (2.05 against 2.01). The flux-loss collapse, however, comes 34 per cent later, the gap opens 62 and 93 per cent later on the two branches, and the branch separation is 36 per cent smaller (0.58 against 0.91 $t_{\rm acc}$). The wind-consistent profile is shallower in the inner disc than the viscous one, and drains correspondingly more slowly. Holding $\tau_B/t_{\rm acc}$ and $t_{\rm end}/t_{\rm acc}$ fixed does not by itself make the outcome dimensionless: the two-branch divide also depends on where the launching region sits relative to the mass, which the two initial profiles place differently. This appendix therefore establishes that the two-branch divide is not an artefact of the low-accretion normalisation adopted

in the main text, not that its magnitude is a universal function of the dimensionless parameters.

One dimensional scale in particular refuses to be absorbed, and it is the reason this run never disperses. The internal photoevaporation rate is set by the X-ray luminosity, not by the disc. $\dot{\Sigma}_{\rm PE}(R)$ is the same absolute profile in both configurations, delivering 5.1 and $5.6\times10^{-10}\,{\rm M}_\odot\,{\rm yr}^{-1}$ after screening, a 10 per cent difference against a factor 5 in disc mass. The local depletion time $\Sigma/\dot{\Sigma}_{\rm PE}$ over 8–40 AU is consequently 26 Myr in the fiducial and 121 Myr here. Once flux loss has collapsed R_β to a few AU, photoevaporation is the only sink left, and at that rate the disc is static on the horizon integrated. It retains 33 per cent of its initial mass at 5.3 Myr, with $\max\Sigma$ still at $29\,{\rm g\,cm^{-2}}$, against the $1\,{\rm g\,cm^{-2}}$ dispersal threshold. The cavity profile of Appendix G never engages either, since it amplifies the loss at an advancing wall and no wall advances. $R_{\rm cav}$ wanders non-monotonically between 3 and 10 AU for the whole run. The implication is a sharper form of the disc-lifetime problem discussed in Section 6.3: at fixed $L_{\rm X}$, internal photoevaporation cannot disperse a massive, high-accretion disc on an observable timescale, because its rate is a stellar property while the mass to be removed is a disc property.

APPENDIX E: INDEPENDENT LITERATURE VALIDATION

We now test the numerical integration against two independent, externally published results, each isolating one core component: the transport solver (Tabone et al. 2022) and the internal photoevaporative sink (Sellek et al. 2024). For each test we adopt the published configuration and switch off all unrelated physics: the magnetothermal wind coupling and the screening among it.

E1 The transport solver: Tabone et al. (2022)

We benchmark against the exact closed-form self-similar solutions for disc mass $M_{\rm D}(t)$ derived by Tabone et al. (2022), which isolates the advective and diffusive operators. We test two families: a constant-$\alpha_{\rm DW}$ "hybrid" family parameterised by the transport ratio $\psi = \alpha_{\rm DW}/\alpha_{\rm SS}$ (their Figure 6), and an evolving $\alpha_{\rm DW}(t) \propto \Sigma_{\rm c}(t)^{-\omega_B}$ family parameterised by the field-decay index ω_B of Section 3.4 (their Figure 7).

Because the wind-drift velocity ($v_{\rm DW} = \frac{3}{2}\alpha_{\rm DW}\epsilon c_{\rm s}$, their eq. 15) and the viscous flux in our integrator are algebraically identical to their formulation, we compute the comparison timescale $t_{\rm acc,0}$ and the exact ejection index $\xi(\psi,\lambda)$ directly from the integrator physics, without fitted parameters. That index is their exact eq. (14), not the $\psi\to\infty$ limit $\xi = 1/[2(\lambda-1)]$ used elsewhere in this paper, so the benchmark does not assume the identity the rest of the model relies on.

As shown in Figure E1, the numerical integration reproduces the analytic $M_{\rm D}(t)$ across all eight parameter regimes, to a median of 0.1–1 per cent in each. The larger excursions are confined to the late-time tail where both curves approach zero mass. The comparison window for finite-ψ runs is truncated once viscous spreading carries the disc beyond the integrator's $\beta_0(R)$ magnetic launch switch (Section 4): a physical constraint present in our numerical setup, set by this paper's own fiducial $\beta_0(R)$ instead of by any free parameter of this comparison, and absent in the idealised analytic model.

E2 The internal photoevaporation sink: Sellek et al. (2024)

To isolate the internal X-ray-driven mass-loss sink, we replicate the plot from Fig. 15 of Sellek et al. (2024). The configuration is a purely viscous disc ($\alpha_{\rm SS} = 10^{-3}$, $\alpha_{\rm DW} = 0$) with a 1 $M_\odot$ star, initial mass 100 $M_{\rm Jup}$, cut-off radius $R_{\rm c} = 100$ AU, and $L_{\rm X} = 2\times10^{30}$ erg s^{-1}, integrated to $t = 10$ Myr. We disable the co-moving screening $R_{\rm c}(t)$ of Picogna & Ercolano (2026) adopted elsewhere in this paper, leaving internal photoevaporation continuous and unscreened as Sellek et al. originally modelled it.

Figure E1 compares our numerical output to the digitised reference curve. The two agree closely over the first 9 Myr, with median offsets of 0.6% in gas mass and 4.7% in accretion rate. They diverge only in the final $\sim$ 1 Myr as the disc depletes, where small timing offsets become large fractional errors near zero mass. This validates the internal sink and the viscous transport term in isolation: the magnetothermal wind, the Ξ–T wind-base prescription and the $R_{\rm c}(t)$ screening used elsewhere in this paper are all inactive here.

APPENDIX F: GRID-RESOLUTION CONVERGENCE

Figure F1 evaluates convergence by doubling the fiducial grid resolution from $N = 512$ to $N = 1024$ (logarithmic spacing). Both resolutions are run to the same per-branch horizon and record snapshots on the same 0.5 Myr grid, so every comparison below is between identical epochs. Across both evolutionary branches, the stellar accretion rate $\dot{M}_*(t)$ overlaps almost perfectly up to terminal collapse, whose epoch shifts by −0.6% (flux-retained) and −0.01% (flux-loss). These are differential shifts measured under the fixed criterion of Section 5.2, not a claim of that precision on the absolute epoch, which that criterion leaves far less well determined.

Prior to collapse, the surface density profiles $\Sigma(R,t)$ agree across the full radial range to a median of 0.6% (2.0 Myr) and 1.3% (3.5 Myr) on the flux-retained branch, and 0.9% and 3.8% on the flux-loss one. The magnetisation front $R_\beta(t)$ is best compared in grid cells, one cell being worth 1.4 per cent in R at $N = 512$ and 0.7 at $N = 1024$. Measured over the whole pre-collapse trajectory rather than at sampled epochs, the two resolutions agree to a median of 0.25 cells on both branches, and lie within one cell for 89 per cent (flux-retained) and 100 per cent (flux-loss) of that trajectory. Because the quantities quoted in the main text are converged at the per-cent level, $N = 512$ is adopted as the fiducial resolution.

F1 What can be trusted near dispersal

Grid convergence degrades only during the terminal collapse phase. Rather than record that as a generic numerical artefact, we set out where it degrades, what the disc is doing there, and why further grid refinement is the wrong tool for it.

The flux-loss branch traverses its dispersal phase fully converged. Its median Σ discrepancy stays below 0.8% at every epoch sampled, and R_β agrees to a median of 0.25 grid cells and stays within a single cell for the full simulation. The flux-retained branch is converged in the same sense over most of its life (also a median of 0.25 cells, and within one cell 89 per cent of the time), but degrades over the approach to collapse. The disagreement exceeds two cells for 3.0 per cent of the pre-collapse trajectory, in brief excursions of 3–109 kyr between $t_{\rm coll} - 0.48$ and $t_{\rm coll} - 0.30$ Myr. These peak at 2.8 cells (3.7 per cent in radius) while the front is sweeping outward from 110 to 140 AU. Local Σ errors reach 16% over the final 0.05 Myr, along the steepest edges of the collapsing density profile. These values are

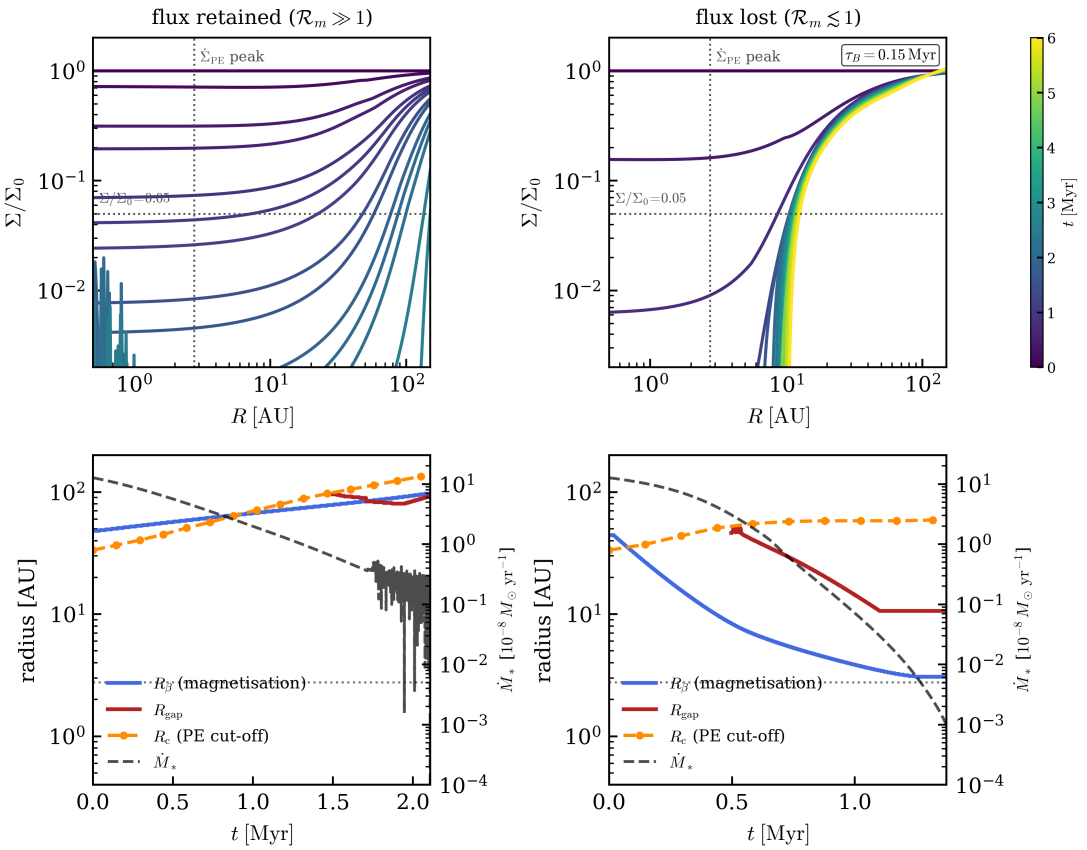

Figure D1. As Fig. 3, but for both branches restarted from the wind-consistent Tabone et al. (2022) initial profile, normalised to the high end of the observed Class II accretion range (17 times the fiducial $\dot{M}_*(0)$), with β_0(1 AU) held so that $R_\beta(0)$ is unchanged, and τ_B and $t_{\rm end}$ rescaled so that the dimensionless control ratios $\tau_B/t_{\rm acc}$ and $t_{\rm end}/t_{\rm acc}$ match Fig. 3's. Holding those ratios fixed does not make the outcome dimensionless, and the appendix text does not claim it does. What this figure tests is that the two-branch divide occurs at all at this accretion rate. Panels and colour scale follow Figure 3: surface density at a regular cadence carried to the end of each run, coloured by the shared bar above, and curves thinned to at most 16 per panel where the stored cadence is finer. Neither branch reaches the 1 g cm^{-2} dispersal threshold within the integrated horizon: at this disc mass the photoevaporative depletion time is a factor ~ 5 longer than in the fiducial, for the reason given in the appendix text. Parameters, and the post-collapse caveats, are given there.

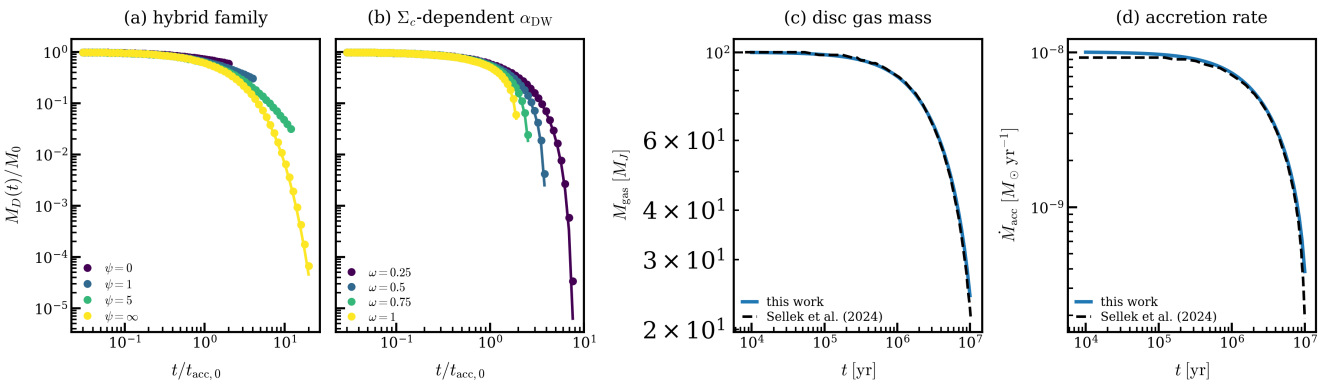

Figure E1. Validation against Tabone et al. (2022) *(a, b)* and Sellek et al. (2024) *(c, d)*. *(a, b)*: disc mass evolution $M_D(t)/M_0$ vs. $t/t_{\rm acc,0}$, this integrator's numerical solution (points) against Tabone et al.'s exact closed-form self-similar solutions (lines): *(a)* their Fig. 6 hybrid family (constant $\alpha_{\rm DW}$) at $\psi = \alpha_{\rm DW}/\alpha_{\rm SS} = 0$ (pure viscous), 1, 5 and ∞ (pure wind); *(b)* their Fig. 7 Σ_c-dependent $\alpha_{\rm DW}(t) \propto \Sigma_c(t)^{-\omega_B}$ family at $\omega_B = 0.25, 0.5, 0.75, 1.0$, each terminating near their predicted finite dispersal time $t_{\rm disp} = 2t_{\rm acc,0}/\omega_B$. *(c, d)*: disc gas mass and stellar accretion rate for the pure-viscous, unscreened configuration of Sellek et al.'s own fig. 15 ("this work" curve), this work (blue) against their published curve (black dashed, digitised). Agreement is at the few-per-cent level (median 0.6%/4.7%) over the first 9 Myr, diverging only in the final ~ 1 Myr as the disc approaches near-complete depletion (see text).

quoted for $N = 512 \rightarrow 1024$, but where the same comparing $N = 256$ to 512 grid cells. So R_β converges at first order in radius.

When the flux-retained branch loses convergence, it retains 0.70% of its initial mass at $t_{\rm coll} - 0.15$ Myr and 0.58% at $t_{\rm coll} - 0.05$, and 80% of the remaining active grid cells (carrying 47% of what mass is left) have dropped below $\Sigma/\Sigma_0 = 10^{-2}$. That threshold is a hard boundary: it is the lower limit of the Sellek et al. (2024) Ξ–T calibration, below which the model reverts to the cold-base fallback of Section 2.2. The β–Σ closure (26) is extrapolated by a comparable margin.[2]

The residual disagreement is largely a phase offset. Comparing the two resolutions at equal time to collapse, as opposed to at equal time, removes most of it. On the flux-retained branch the median Σ discrepancy falls from 9.2 to 2.3 per cent at $t_{\rm coll} - 0.15$ Myr, and from 16.4 to 0.7 per cent at $t_{\rm coll} - 0.05$. The two grids therefore evolve through nearly the same sequence of states and reach them at slightly different times, instead of diverging onto different solutions.

Grid refinement is not the remedy. On the flux-loss branch the dispersal epoch is definition-limited, as opposed to grid-limited, by a wide margin. Doubling the resolution moves it by 0.5 kyr, whereas moving the $\dot{M}_*$ collapse criterion from 10^{-10} to 10^{-13} $M_\odot$ yr^{-1} moves it by 963 kyr, a factor of 1800. On the flux-retained branch refinement moves the epoch by 40 kyr and would buy something. What it would not buy is the thing that limits the answer. Inside the terminal window the physical closures are being extrapolated decades outside their calibrated density range, so a numerically converged result there is a more precise solution to the wrong equations.

We therefore make no quantitative claims about the terminal 0.3 Myr of the flux-retained branch, nor about its post-collapse plateau. What the paper does quote (the dispersal epochs to two significant digits with their criterion range attached, the branch separation, the sustained accretion rates, and $\Sigma(R, t)$ and the front trajectories outside that window) is extracted exclusively from the converged windows, and is converged there at the per-cent level or better. It is also differential, in a way that makes the residual sensitivity common to both branches. The two-branch divide the paper rests on is therefore unaffected even where the absolute epochs are not well determined.

APPENDIX G: THE MASS-LOSS PROFILE AT A CAVITY WALL

The photo-evaporative profile applied above is the one computed for a full disc, held fixed for all time. That is the right choice while the disc is primordial, and it brakes down once a cavity has opened. The cavity wall is directly illuminated, and the mass-loss rate per unit area there is enhanced over the primordial value at the same radius. Picogna et al. (2019)-family radiation-hydrodynamic calculations of transition discs (Picogna et al., in prep.) give that enhancement as a function of the wall radius $R_{\rm cav}$. Expressed as a local, dimensionless ratio to the primordial profile at the same radius, it is

$$E(u) = 1 + 5.0\,(u-1)^{-0.23}\exp[-(u-1)/0.15]\,, \qquad u \equiv R/R_{\rm cav}, \quad \text{(G1)}$$

applied for $R_{\rm cav} \le R < 2R_{\rm cav}$, with $\dot{\Sigma}_{\rm PE} = 0$ inside the wall and the primordial profile recovered exactly beyond . The enhancement is sharply confined, which is the behaviour Monsch et al. (2021, their Figure A.1) report for the same family of calculations, showing the profile returning to the primordial one just outside the wall. It peaks at 11–14× the primordial rate at the wall itself, nearly independently of $R_{\rm cav}$, while raising the integrated rate by only 2–27 per cent over the range of cavity radii sampled.

E is a ratio measured against the Picogna et al. (2019) primordial profile but applied here to the Sellek et al. (2024) one. The two peak within 0.5 AU of each other (3.2 against 2.8 AU), which is what makes the transfer defensible, but their integrated rates differ by a factor 9.4. Figure G1 shows the fit of equation (G1) overlayed on the mass-los rates derived from the hydrodynamic numerical simulations (Picogna et al., in prep.), which we publish alongside the rest of this paper's archived data (Data availability).

On both branches a genuine density cavity forms well before the accretion collapse (at $t = 2.05$ Myr on the flux-loss branch and 3.74 Myr on the flux-retained one, see Section 5.2), and outside the terminal window Appendix F1 excludes. Its effect on the clearing is significant. Repeating the flux-loss integration with equation (G1) active and nothing else changed, the cavity wall advances at 5.3 ± 0.3 AU Myr^{-1} against 1.7 ± 0.1 with the primordial profile, over the common window 3.8–5.5 Myr in which both runs have a cavity. At matched epochs the ratio of the two cavity radii grows from 1.4 at $t = 4.1$ Myr to 1.9 at 5.5 Myr, so the difference is still widening when the comparison ends. The retained mass, by contrast, differs by only 2.6 percentage points at 5.5 Myr (23.5 against 26.1 per cent). The cavity-edge enhancement therefore changes where the gas is removed far more than how much is removed. This is what equation (G1) predicts, since it raises the integrated rate by at most a few tens of per cent while amplifying the local rate at the wall by an order of magnitude.

This paper has been typeset from a TEX/LATEX file prepared by the author.

[2] The flux-loss branch escapes this: 36% of its cells are also sub-floor at collapse, but they carry only 0.1% of the remaining gas mass and so are dynamically irrelevant. What matters is not how many cells are extrapolated but how much mass they hold.

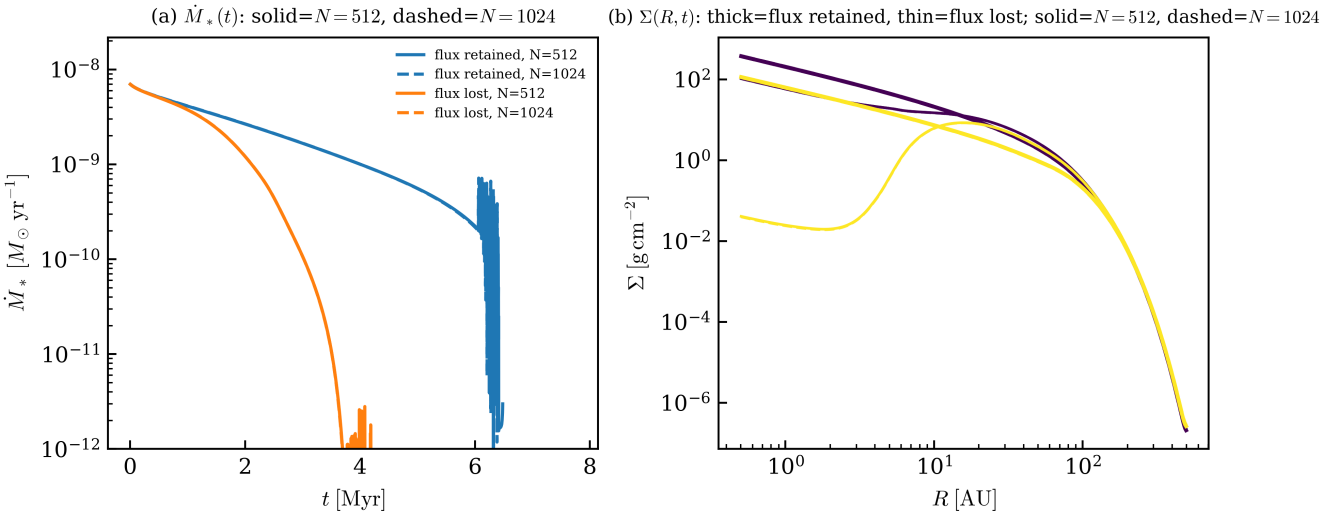

Figure F1. Grid-resolution convergence, $N = 512$ (fiducial) vs. $N = 1024$, log spacing, for both named branches of Figure 3. *Left:* $\dot{M}_*(t)$ (solid: $N = 512$; dashed: $N = 1024$; blue: flux retained; orange: flux lost), with the ordinate floored at 10^{-12} $M_\odot$ yr^{-1}. Below the collapse criterion both resolutions oscillate over many decades on gas carrying negligible mass, and that range is excluded from interpretation in any case (Appendix F1). The structure retained just above the floor near 6.5 Myr is not numerical scatter but the threshold re-crossing described in Section 5.2, which is why the collapse epoch is quoted with a criterion attached. *Right:* $\Sigma(R, t)$ at $t = 2.0$ and 3.5 Myr (thick: flux retained; thin: flux lost; solid: $N = 256$; dashed: $N = 512$). Both epochs are pre-collapse on both branches, and the two resolutions record snapshots on a common 0.5 Myr grid, so each pair compares identical times.

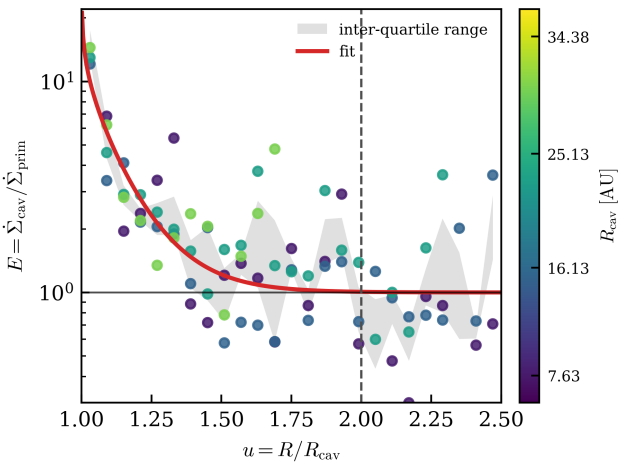

Figure G1. Equation (G1) (red) against the four transition-disc runs it is fitted to (coloured points, $R_{\rm cav}$ = 7.6–34.4 AU), each measured as the ratio of the cavity run's mass-loss rate to the primordial run's at the same radius, binned in $u = R/R_{\rm cav}$. The shaded band is the inter-quartile range across runs at each u; the dashed line marks $u = 2$, beyond which the profile reverts to the primordial one by construction.